MSc in Physics

Experimental implementation of a Top Hat beam shaper

Towards improving the 'light-atom' quantum interface

Isaac Roca Caritg

Supervised by Prof. Eugene S. Polzik

May 20, 2022

Isaac Roca Caritg
Experimental implementation of a Top Hat beam shaper
MSc in Physics, May 20, 2022
Supervisor: Prof. Eugene S. Polzik

University of Copenhagen
QUANTOP, Faculty of Physics
Masters Degree in Phyisics
Niels Bohr Institute, Blegdamsvej 17
2100 København Ø

Acknowledgements

First of all, I would like to express my gratitude to my thesis supervisor Professor Eugene S. Polzik, for giving me the opportunity to participate in the experiments at QUANTOP for my master's thesis project and for his guidance all over these nine months.

I am, in particular, very thankful to Rebecca Schmieg, who mentored me around the lab and helped me with all the theoretical comprehension of my work and the practical realisation. Also, she provided me with very useful comments when I was writing the thesis.

I would like to thank all the people at QUANTOP for creating such a great working environment. Especially Jun Jia, with whom I extensively discussed the ins and outs of beam shaping. Also, Christian F. Bærentsen for providing me with his program for the collimation of the top hat.

I would like to show my gratitude to my friends and family for supporting me during the whole process. Distinctly, Alicia Mosquera, Arnau Morancho and Tomás Fernandez.

Last but not least, I would like to make a special mention to my friends and office mates Beñat Martínez de Aguirre and Alan Oesterle for their comradeship, help and funny moment in the office.

Thank you.

Abstract

On-demand single-photon sources at room-temperature are attractive due to their potential scalability and experimental simplicity compared to their ultracold analogues. However, their performance is not at the same level. Single-photon sources based on the DLCZ scheme with an anti-relaxation coated caesium vapour cells require the use of *motional averaging* to store collective excitations efficiently. Shaping the driving light to a squared *Top Hat* beam with a homogeneous light distribution will increase the filling factor between the light and the atomic ensemble and speed up the motional averaging.

In this thesis, we aim to implement a Top Hat beam shaper to a fundamental Gaussian beam (TEM_{00}). The reshaping is performed using a *Diffractive Optical Element* which produces a squared profile with homogeneous power distribution at the focal plane of a focusing system. Furthermore, a second lens allows for the collimation of the flat profile along 180 mm under the proper conditions.

This work also includes the characterisation of the new batch of vapour cells created. The *cell characterisation* consists of several tests that return the main features of the vapour cell: its atomic density, the transmission of the light through the cell, and the relaxation times.

Keywords: Top Hat profile, Beam shaping, motional averaging, cell characterisation.

Contents

List of Figures

List of Tables

List of abbreviations and Table of constants

Table 0.1.: List of abbreviations

Abbreviation	Name
AOM	Acousto-Optical Modulator
APD	Avalanche Photodetector
AR	Anti-Reflective
BS	Beamsplitter
BPD	Balanced Photodetector
CSS	Coherent Spin State
DOE	Diffractive Optical Element
ECDL	External Cavity Diode Laser
EFL	Effective Focal Length
EOM	Electro-Optical Modulator
FWHM	Full Width Half Maximum
HWP	Half-Wave Plate
MORS	Magneto-Optical Resonance Spectroscopy
MZI	Mach-Zehnder Interferometer
PBS	Polarizing Beamsplitters
PD	Photodetector
PSD	Power Spectral Density
QWP	Quarter-Wave Plate
STD	Standard deviation
TH	Top Hat

Table 0.2.: Table of constants

Symbol	Name	Value
μ_B	Bohr Magneton	$h \cdot 1.399624604(35)$ MHz G^{-1}
h	Plank constant	$4.13566733(10) \times 10^{-15}$ eV s
$\hbar$	Reduced Plank constant	$6.58211899(16) \times 10^{-16}$ eV s
c	Velocity of light	2.99792458×10^{8} m s^{-1}
ϵ_0	Permittivity of Vacuum	$8.854187817 \times 10^{-12}$ F m^{-1}
γ_{D_2}	Decay rate D$_2$-line	$2\pi \cdot 5.234(13)$ MHz
r_e	Electron radius	$2.8179403262 \times 10^{-15}$ m
f	Oscillator strength D$_2$-line	$0.7164(18)$
e	Elementary charge	$1.602176487(40) \times 10^{-19}$ C

Introduction

'Light-atomic ensembles' quantum interfaces have been proven to be a robust tool for quantum technologies [1–7]. For quantum communication, it is essential to be able to store (write) and retrieve (read) information efficiently from the quantum system [3]. Therefore, ultracold atomic ensembles have been considered for their exceptional performance [3, 5]. However, room-temperature atomic ensembles are easier to work with and are especially attractive due to their scalability since they do not require extended cooling devices [3, 5].

Room-temperature atomic ensembles contained in vapour cells are a building block in the experiments in our laboratories. They have been proven to be very useful in fields such as magnetometry [1], quantum teleportation [2], quantum memory [4], single-photon sources [5], and entanglement [7].

Vapour cells are attractive due to their high performance in, for example sensing technologies or non-classical light sources [8], yet they are a relatively simple system [3]. Our vapour cells consist of a glass container filled with Caesium atoms. To prevent the spin decoherence induced by the collisions of the atoms with the walls, the cells are coated with an anti-relaxation coating. It has been shown in [9] that coated vapour cells can allow for spin coherences on the order of minutes.

As mentioned before, writing and reading information are crucial for quantum communication. The 'write' process starts after preparing all the atoms in the ground state, $|0\rangle$. Then, we rely on creating a single collective excitation of the ensemble, which can be represented by the symmetric Dicke state [6]

$$|\psi_D\rangle = \frac{1}{\sqrt{N}} \sum_j |1\rangle_j \langle 0| |00\ldots0\rangle \tag{1.1}$$

where j represents the j-th atom, N is the number of atoms, and $|0\rangle$ and $|1\rangle$ are the two ground states of the atoms. In the 'write' process, an atom is excited to a far detuned excited level $|e\rangle$, which is coupled to the state $|1\rangle$ emitting a photon and projecting the atomic state into $|\Psi_D\rangle$ [3].
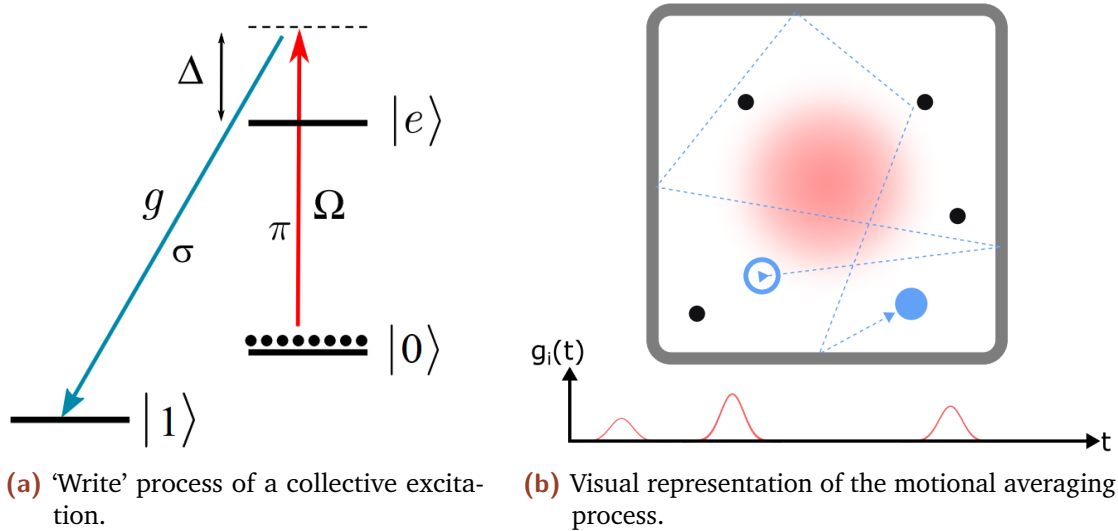
(a) 'Write' process of a collective excitation.

(b) Visual representation of the motional averaging process.

Figure 1.1.: In (a) 'Write' process of a collective excitation. The excitation $|0\rangle \rightarrow |e\rangle$ is far detuned Δ. In (b) Atoms bouncing inside a cell shined by a Gaussian laser (red spot). The black dots represent other single atoms. The coupling of the atom with the light is represented by $g_i(t)$
Pictures extracted from [8].

The problem with room-temperature atomic ensembles is the intrinsic motion of the atoms. In an experimental setup, lasers have a thinner width than the ensemble volume. The movement of the atoms with the inhomogeneous distribution of light of a Gaussian beam causes an uneven light-atom interaction, which leads to an asymmetric state [3]. But, as the cell walls are anti-relaxation coated, the atoms bounce into the wall without losing their atomic state. After bouncing, they may cross the beam (again). After a long enough time, all the atoms would have experienced the same interaction with the light [3]. We refer to this effect as *motional averaging*.

In the proposal of 'scalable quantum interfaces based on motional averaging in room-temperature ensembles', made by [3] and explored, e.g. in [8, 10] the following experimental setup is proposed. A Caesium atomic ensemble is contained in an anti-relaxation coated microcell of $2L \times 2L \times L_z$ with $2L = 0.3$ mm and $L_z = 10$ mm. To enhance the interaction with light, the cell is placed in a single-sided optical cavity referred to as 'cell-cavity'. In addition, an external filter cavity is placed to separate the emitted quantum photon from the classical light of the beam. A 'written' excitation can afterwards be read out during the read-out process by driving a pulse in $|1\rangle \rightarrow |e\rangle$ transition such that the excitation is converted into a photon in the transition $|e\rangle \rightarrow |0\rangle$.
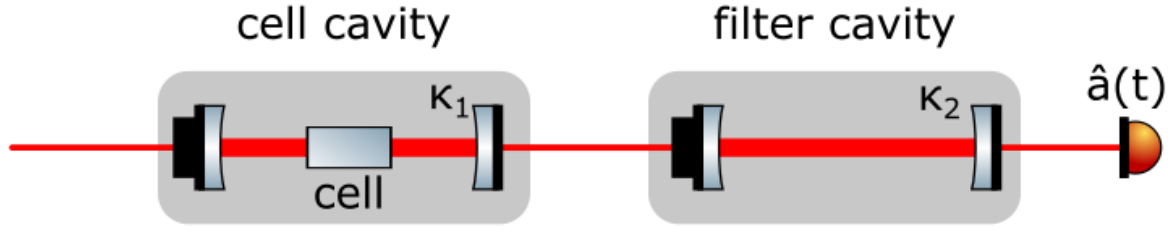
Figure 1.2.: Schematic of the setup described in Borregaard, Zugenmaier, Petersen, Shen, Vasilakis, Jensen, Polzik, and Sørensen. κ_1 and κ_2 are the cell-cavity and the filter cavity decay rates, respectively. $\hat{a}(t)$ described the field in the detector. Figure extracted from [10].

The efficiency of the 'write' process can be written as [3]

$$\eta_W = \left[1 + \frac{k_2}{2\Gamma + k_2} \left(\frac{4L^2}{\pi w^2} - 1 \right) \right]^{-1} \tag{1.2}$$

Where k_2 and Γ are the decay rates of the filter cavity and the excited photon and atomic position correlations [3]. The term $\dfrac{\pi w^2}{4L^2}$ describes the beam cross-section and channel size ratio. It is often referred to as the *filling factor*. This equation shows that $\eta_W \to 1$ when $\dfrac{k_2}{\Gamma} \to 0$ and when $\dfrac{4L^2}{\pi w^2} \to 1$ where w is half the waist of the beam. That is, the writing efficiency improves with the duration of the effective interaction time and when the beam covers more area of the cell area [3].

As shown in Figure 1.3, the output of the cell-cavity is formed by two different spectral components [8]:

1. A narrowband component associated to the long coherent interaction of the atoms with the beam (symmetric collective excitations).

2. A broadband component associated to incoherent asymmetric contributions.

In [8], Dideriksen pointed out some possible improvements to the described setup:

- The main limiting factor in the coherence time are the collisions with the cell's wall. Therefore, a bigger cross-section would increase the time between collisions, which would increase the coherence time of the spin state.

- The utilisation of a Top Hat (TH) profile. The uniformity of a TH profile would increase the effective filling factor speeding up the motional averaging.

- The removal of the cell cavity. The cell cavity limits the overall efficiency. Additionally, the TH configuration and the cell cavity are not compatible.
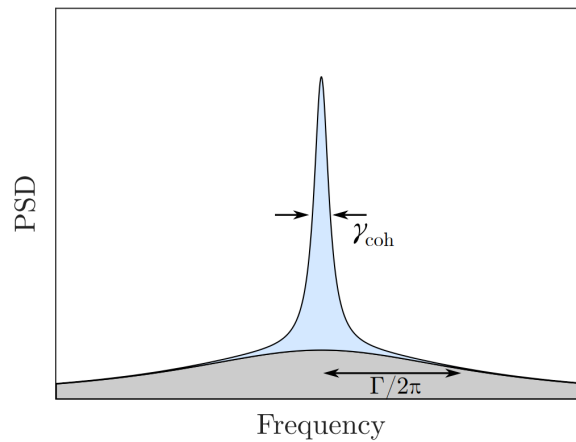
Figure 1.3.: Power spectral density (PSD) of the writing process. It consists of a narrowband associated with the symmetric collective excitations, and a broadband associated with incoherent asymmetric contributions due to insufficient motional averaging [5].
Figure extracted from [8].

Hence, for the future incarnation of this experiment, we chose to implement a new larger cell combined with a TH beam profile. A larger optical depth will enhance the light-atom interaction. These proposals guided the development of this thesis.

My work

This thesis will discuss the characterisation of new fabricated cells that fit our specifications. Characterising the features of new vapour cells is an essential requirement. The techniques used are well known in the lab. Taking advantage of the visit of the Assoc. Prof. Mikhail Balabas of Saint-Petersburg State University, the producer of our Caesium anti-relaxation coated vapour cells, we requested different kinds of cells fitting all the experiments in our lab. The characterisation of all these cells is covered in Part I.

Part II will cover the implementation of the Top Hat profile using a diffractive beam shaper. First, it will cover the creation of a squared flat profile from a fundamental Gaussian mode, its proper alignment, and an exhaustive analysis to determine its size, main intensity, and quality. Afterwards, an introduction to the collimation of the TH profile will be given. The Top Hat implementation was the central part of my project, where I spent most of the time during the thesis.

At the end of the thesis, some concluding statements and future prospects will be stated.

Part I

Cell Characterisation

Theoretical background | 2

This chapter will introduce the theoretical background necessary to understand the cell characterisation.

First, the atomic properties of Caesium will be explained in section 2.1. Then, the interaction with light with an atomic ensemble and its dynamics equations are introduced in section 2.2. The following sections describe the theoretical background used to characterise the cells. Namely, the atomic density in section 2.3, the Faraday effect in section 2.4 and the magneto-optical resonance in section 2.5. Finally, spin relaxation times are introduced in section 2.6.

2.1 Caesium atom

In the experimental setups, we use caesium vapour cells as atomic ensembles. In this section, we shall introduce the caesium atom.

The caesium atom (Cs) is an alkali element with only one valence electron. Its only stable isotope is ^{133}Cs with a nuclear spin of $\mathbf{I} = 7/2$. Caesium's electronic configuration can be written as $[Xe]\, 6s^1$, which means its only valence electron occupies the $6^2S_{1/2}$ orbital. This energy level is described with the spectroscopic notation $n^{2\mathbf{S}+1}\mathbf{L_J}$, where n is the principal quantum number, $\mathbf{L}$ is the orbital angular momentum ($S \rightarrow \mathbf{L} = 0$), $\mathbf{J}$ is the total electronic angular momentum, $\mathbf{S}$ is the electron spin, and $2\mathbf{S} + 1$ denotes the multiplicity. $\mathbf{J}$ is described by $\mathbf{J} = \mathbf{L} \pm \mathbf{S}$. The electron spin of Cs' only valence electron is $\mathbf{S} = 1/2$.

The ground state of the Cs splits into two hyperfine manifolds characterised by the quantum number $\mathbf{F} = \mathbf{I} \pm \mathbf{J}$, which is the total angular momentum. This leads to $\mathbf{F} = 3$ and $\mathbf{F} = 4$.

Our experiments work only with transitions to the first excited states $6^2P_{1/2}$ and $6^2P_{3/2}$ ($\mathbf{L} = 1$). The transition $6^2S_{1/2} \rightarrow 6^2P_{1/2}$ is referred to as D_1 with a wavelength of $\lambda = 895$ nm. The one from $6^2S_{1/2} \rightarrow 6^2P_{3/2}$ is referred to as D_2 with a wavelength of $\lambda = 852$ nm. Similar to the ground state, both excited states split into hyperfine levels. Two ($F = \{3, 4\}$) for $6^2P_{1/2}$ and four ($F = \{2, 3, 4, 5\}$) for $6^2P_{3/2}$.

Each hyperfine level has $|2\mathbf{F} + 1|$ magnetic sublevels, and its degeneracy is lifted when applying a magnetic field. This effect is called *Zeeman splitting*. These sublevels are

characterised by the magnetic quantum number $m_F = \{-F, -F+1, ..., F-1, F\}$. m_F describes the projection onto the field's orientation with magnitude B. The energy shift of these sublevels is given in [11] by

$$\Delta E_B = \mu_B g_F m_F B \tag{2.1}$$

Where μ_B is the Bohr magneton, and g_F is the Landé g-factor. For low magnetic field, the Zeeman effect splits the hyperfine manifolds into equidistant sublevels. At room temperature, the Cs atoms are equally distributed in the magnetic sublevels. The magnetic sub-levels can be represented in the Dirac notation as $|F, m_F\rangle$.
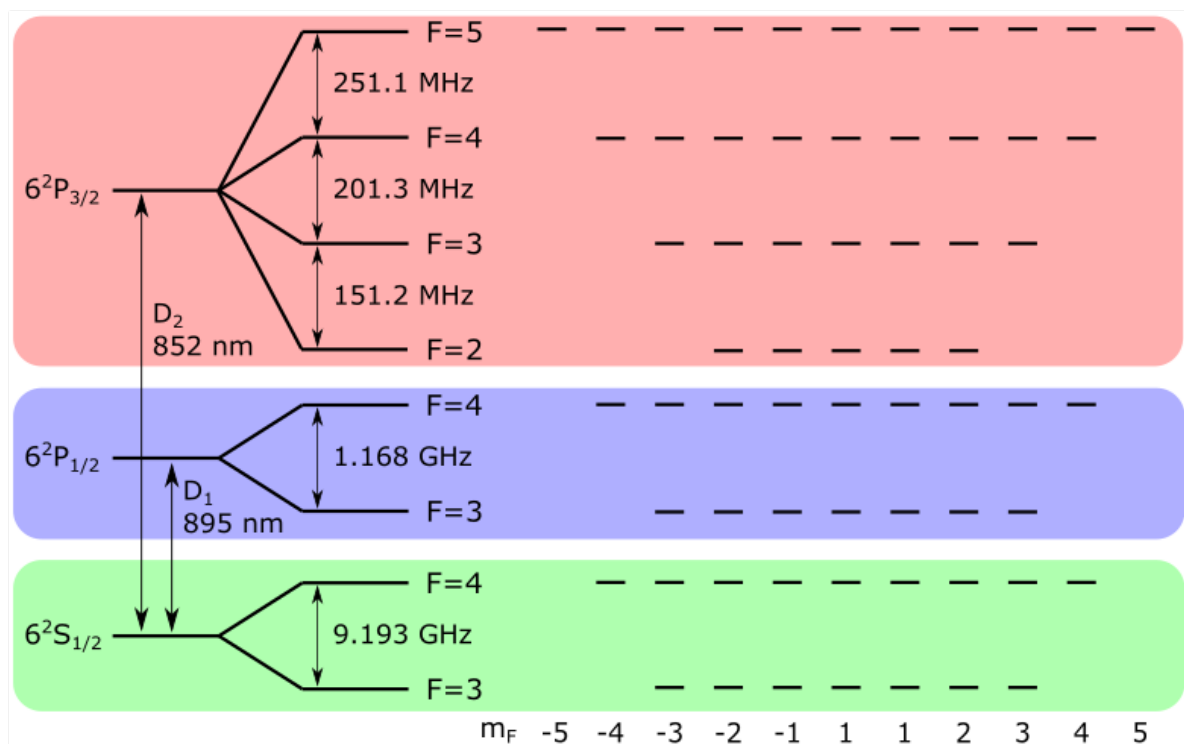
Figure 2.1.: Caesium level structure for the ground state and the two first excited states, including hyperfine and Zeeman splitting. Data taken from [12]. Figure adapted from [8].

2.1.1 Atomic spin operators

As we will see later in section 4.5, in our experiments, we work with atomic ensembles of $\sim 10^7 - 10^{10}$ atoms, which makes it difficult to keep track of their dynamics. Hence, we will define some collective operators to describe the collective properties of the atomic ensemble. In literature, **J** is usually used to describe the total angular momentum of the ensemble (*collective spin*) [13]. But, as we use it to describe the

orbital angular momentum, we will use $\hat{\mathcal{J}}$. With this new notation in mind, the collective spin can be defined as

$$\hat{\mathcal{J}} = \sum_{i=1}^{N_a} \mathbf{F}_i \tag{2.2}$$

Where N_a is the number of atoms in the ensemble and $\mathbf{F}_i$ is the total angular momentum of the i-th single atom. This total momentum has projections operators in the three Cartesian axis, $\hat{\mathcal{J}}_x$, $\hat{\mathcal{J}}_y$ and $\hat{\mathcal{J}}_z$ [14]. These operators satisfy the commutation relations

$$\left[\hat{\mathcal{J}}_j, \hat{\mathcal{J}}_k\right] = \epsilon_{jkl} i \hat{\mathcal{J}}_l \tag{2.3}$$

and the Heisenberg uncertainty principle [15]

$$\text{Var}\left(\hat{\mathcal{J}}_y\right) \text{Var}\left(\hat{\mathcal{J}}_z\right) \geq \frac{\hat{\mathcal{J}}_x^2}{4} \tag{2.4}$$

In the case all the atoms are oriented in one direction creating a *coherent spin state*, CSS, (e.g. all the atoms in the $F = 4$ are in the Zeeman sublevel $m_F = 4$), we can treat the collective spin in that direction as a macroscopic spin with a classical number. Since we define our quantisation axis to be the x- axis, $\hat{\mathcal{J}}_x \to \mathcal{J}_x$. In this case, Equation 2.4 will be equalised. When

$$\text{Var}\left(\hat{\mathcal{J}}_y\right) = \text{Var}\left(\hat{\mathcal{J}}_z\right) = \frac{S_x}{2} \to \text{Var}\left(\hat{\mathcal{J}}_y\right) \text{Var}\left(\hat{\mathcal{J}}_z\right) = \frac{S_x^2}{4} \tag{2.5}$$

we call the atomic noise to be at the fundamental *projection noise level*.

2.2 Light-Atom interaction

In order to describe light-atom interaction, we need to have a formalism to describe light section 2.2.1 and atoms section 2.2.2, in order to develop a notation for the combined system section 2.2.3.

2.2.1 Polarisation states of light

The experiments in our lab involve light interacting with atomic ensembles. To describe the polarisation states of light, we use the *Stokes operators* [16]. For light propagating along the z-direction

$$\hat{S}_x = \frac{1}{2}\left(\hat{n}_x - \hat{n}_y\right) \tag{2.6}$$

$$\hat{S}_y = \frac{1}{2}\left(\hat{n}_{+45°} - \hat{n}_{-45°}\right) \tag{2.7}$$

$$\hat{S}_z = \frac{1}{2}\left(\hat{n}_{\sigma_+} - \hat{n}_{\sigma_-}\right) \tag{2.8}$$

Where the operator $\hat{n}_i$ indicates the number of photons in a certain direction i. With these operators it can also be defined the *photon flux operator* as

$$\hat{\phi}(z,t) = \hat{n}_x + \hat{n}_y = \hat{n}_{+45°} + \hat{n}_{-45°} = \hat{n}_{\sigma_+} + \hat{n}_{\sigma_-} \tag{2.9}$$

These operators count the number of photons in a beam. The flux operator commutes with the other Stokes operators. The Stokes operators satisfy the following commutation and uncertainty relations [14]

$$\left[\hat{S}_j, \hat{S}_k \right] = \epsilon_{jkl} i \hat{S}_l \tag{2.10}$$

$$\text{Var}\left(\hat{S}_y \right) \text{Var}\left(\hat{S}_z \right) \geq \frac{\hat{S}_x^2}{4} \tag{2.11}$$

If we assume all the photons in our light pulse to be x-polarised, then any photon would be y-polarised (vacuum state), and Equation 2.11 will be equalised. As all the photons are polarised along the x-direction, we can do the substitution $\hat{S}_x \to S_x$. When

$$\text{Var}\left(\hat{S}_y \right) = \text{Var}\left(\hat{S}_z \right) = \frac{S_x}{2} \to \text{Var}\left(\hat{S}_y \right) \text{Var}\left(\hat{S}_z \right) = \frac{S_x^2}{4} \tag{2.12}$$

we call the light to be at *shot-noise level*.

2.2.2 Interaction Hamiltonian

To describe the dynamics of the atoms, we have first to describe the interaction of the atomic ensemble with light. This interaction is detailed in the *effective interaction Hamiltonian*, $\hat{H}_I^{eff}$. This Hamiltonian has been thoroughly derived by Julsgard in [13], so we will just briefly depict it.

The effective interaction Hamiltonian describing the interaction of an ensemble in the $6S_{1/2}$, $F = 4$ ground stated with a light far detuned from the D_2-line propagating along the z-axis, can be expressed as [13]

$$\begin{aligned}
\hat{H}_{\text{int}}^{\text{eff}} = -\frac{\hbar c \gamma}{4A\Delta} \frac{\lambda^2}{2\pi} \int_0^L \Big(& a_0 \cdot \hat{\phi}(z,t) + a_1 \cdot \hat{S}_z(z,t)\hat{F}_z(z,t) \\
& + a_2 \left[\hat{\phi}(z,t)\hat{F}_z^2(z,t) - \hat{S}_-(z,t)\hat{F}_+^2(z,t) - \hat{S}_+(z,t)\hat{F}_-^2(z,t) \right] \Big) \rho A dz
\end{aligned} \tag{2.13}$$

Where γ is the decay rate (Full width half maximum, FWHM, of the $6P_{3/2}$ excited state) and can be expressed as $\gamma = 2\pi \cdot 5.21$ MHz, λ is the wavelength of the light, Δ the detuning of the light, A is the cross-section of the atomic ensemble and ρ is the atomic density. a_0, a_1 and a_2 are dimensionless parameters that depend on the

detuning. For $F = 4$ is the light is far blue-detuned $a_0 \to 4$, $a_1 \to 1$ and $a_2 \to 0$. Where $\hat{S}_j$ are the Stokes operators with dimension m^{-1} and $\hat{F}_j$ are the total angular momentum operators that are dimensionless. j represents the projection direction in the Cartesian axis x, y or z. '+' and '−' represent the vector on circular basis, which may be expressed as, in the case of the Stokes vector,

$$\hat{S}_+ = \hat{S}_x + i\hat{S}_y \tag{2.14}$$

$$\hat{S}_- = \hat{S}_x - i\hat{S}_y \tag{2.15}$$

These operators, obey the following commutation relations [14]

$$\left[\hat{S}_j(z,t), \hat{S}_k(z',t)\right] = \epsilon_{jkl}\delta(z-z') i\hat{S}_l(z,t) \tag{2.16}$$

$$\left[\hat{F}_j(z,t), \hat{F}_k(z',t)\right] = \epsilon_{jkl}\frac{1}{\rho A}\delta(z-z') i\hat{F}_l(z,t) \tag{2.17}$$

In the Hamiltonian in Equation 2.13, the first term describes a *Stark shift*[1] proportional to the photon flux. The second term rotates around the z-axis the Stokes vector $\hat{\mathbf{S}}$ and the spin vector $\hat{\mathbf{F}}$ (total angular momentum of a single atom). The last term describes high-order light-atom interaction [13].

Under these conditions, the Hamiltonian can be reduced to

$$\hat{H}_{\text{int}}^{\text{eff}} = -\frac{\hbar c\gamma}{4A\Delta}\frac{\lambda^2}{2\pi}\int_0^L \left[a_0 \cdot \hat{\phi}(z,t) + a_1 \cdot \hat{S}_z(z,t)\hat{F}_z(z,t)\right] dz \tag{2.18}$$

2.2.3 Equations of motion

To obtain the dynamics of our system, we want the equations of motion of the spin operators $\hat{\mathbf{F}}$ and the Stokes operators $\hat{\mathbf{S}}$.

The equations of motion of the spin operators can be obtained by solving the *Heisenberg equation* [15]

$$\frac{\partial \hat{\mathbf{F}}(z,t)}{\partial t} = -\frac{i}{\hbar}\left[\hat{\mathbf{F}}(z,t), \hat{H}_I^{\text{eff}}\right] \tag{2.19}$$

---

1. The *Stark shift* is a shift in the energy levels produced by a perturbing radiation[11] (e.g. the incident light to the atomic ensemble).

which leads to

$$\frac{\partial \hat{F}_x(z,t)}{\partial t} = a_1 \frac{c\gamma\lambda^2}{16\pi A\Delta} \hat{S}_z(z,t)\hat{F}_y(z,t) \tag{2.20}$$

$$\frac{\partial \hat{F}_y(z,t)}{\partial t} = -a_1 \frac{c\gamma\lambda^2}{16\pi A\Delta} \hat{S}_z(z,t)\hat{F}_x(z,t) \tag{2.21}$$

$$\frac{\partial \hat{F}_z(z,t)}{\partial t} = 0 \tag{2.22}$$

For commodity, we will define $C = -a_1(c\gamma\lambda^2)/(16\pi A\Delta)$. From this equation, it can be seen that the z component is constant, and the spin will suffer a rotation on the $x-y$ plane proportional to the Stokes operator $\hat{S}_z$. Now we redefine the collective spin in each direction as

$$\mathcal{J}_j = \int_0^L \hat{F}_j(z,t)\,\rho A dz \tag{2.23}$$

for $j = x, y, z$. If we consider the incident light linear polarised in one axis, e.g. x-axis, the Stokes and the spin operators in the x will not vary much from this situation. In this case, we can substitute the operators for macroscopic quantities ($\hat{S}_x \to S_x$, $\hat{\mathcal{J}}_x \to \mathcal{J}_x$) [17].

Then, the motion equations for the collective spin are reduced to

$$\frac{\partial \hat{\mathcal{J}}_y(z,t)}{\partial t} = C\hat{S}_z(z,t)\mathcal{J}_x(z,t) \tag{2.24}$$

$$\frac{\partial \hat{\mathcal{J}}_z(z,t)}{\partial t} = 0 \tag{2.25}$$

For the Stokes operators, we can rewrite the Heisenberg equation as [14]

$$\left(\frac{\partial}{\partial t} + c\frac{\partial}{\partial z}\right)\hat{\mathbf{S}}(z,t) = -\frac{i}{\hbar}\left[\hat{\mathbf{S}}(z,t), \hat{H}_I^{\text{eff}}\right] \tag{2.26}$$

To simplify these equations, we will neglect the retardation effects of $\dfrac{\partial}{\partial t}$ by taking $c \to \infty$ [17]. This leaves us with the following motion equations

$$\frac{\partial \hat{S}_x(z,t)}{\partial z} = a_1 \frac{\gamma\lambda^2\rho}{16\pi\Delta} \hat{S}_y(z,t)\hat{\mathcal{J}}_z(z,t) \tag{2.27}$$

$$\frac{\partial \hat{S}_y(z,t)}{\partial z} = -a_1 \frac{\gamma\lambda^2\rho}{16\pi\Delta} \hat{S}_x(z,t)\hat{\mathcal{J}}_z(z,t) \tag{2.28}$$

$$\frac{\partial \hat{S}_z(z,t)}{\partial z} = 0 \tag{2.29}$$

To solve this equation, we will define the input/output operators, which describe the state of the Stoke operator before crossing the atomic ensemble and after respectively [14]

$$c\hat{S}_i(0, t) \equiv \hat{S}_i^{\text{in}} \tag{2.30}$$

$$c\hat{S}_i(L, t) \equiv \hat{S}_i^{\text{out}} \tag{2.31}$$

This new operators have the dimension s^{-1}. From the equations of motion we see that the z is constant so the input and the output will be the same. The coupled differential equations for the x and y component can be solved as [14]

$$\hat{S}_x^{\text{out}}(t) = \hat{S}_x^{in}(t) \cos 2\theta_F - \hat{S}_y^{in}(t) \sin 2\theta_F \tag{2.32}$$

$$\hat{S}_y^{\text{out}}(t) = \hat{S}_y^{\text{in}}(t) \cos 2\theta_F + \hat{S}_x^{in}(t) \sin 2\theta_F \tag{2.33}$$

$$\hat{S}_z^{\text{out}}(t) = \hat{S}_z^{\text{in}}(t) \tag{2.34}$$

Where we see that the Stokes operators suffer rotated along the propagation axis of the light (i.e. z-axis) with an angle

$$\theta_F = -a_1 \frac{\gamma \lambda^2 \rho L}{32\pi\Delta} \langle \hat{\mathcal{J}}_z(z, t) \rangle \tag{2.35}$$

Now, if we make the same assumption that before and consider the light to be linearly polarised along the x-axis and the collective spins, we can reduce the equations of motion to

$$\frac{\partial \hat{\mathcal{J}}_y(t)}{\partial t} = C\hat{S}_z^{\text{in}}(t)\mathcal{J}_x(z, t) \tag{2.36}$$

$$\frac{\partial \hat{\mathcal{J}}_z(t)}{\partial t} = 0 \tag{2.37}$$

$$\hat{S}_y^{\text{out}}(t) = \hat{S}_y^{\text{in}}(t) + CS_x\hat{\mathcal{J}}_x(t) \tag{2.38}$$

$$\hat{S}_z^{\text{out}}(t) = \hat{S}_z^{\text{in}}(t) \tag{2.39}$$

2.2.4 Rotation Frame

If we apply a homogeneous magnetic field $\mathbf{B}$ along the x-direction (could be any direction), the energy levels will split into the Zeeman magnetic sublevels and cause the so-called *Larmor precession*. The Larmor precession describes a spin precession along the direction of the magnetic field with frequency Ω (Larmor frequency).

The magnetic field contribution to the Hamiltonian is

$$\hat{H}_{\mathbf{B}} = \hbar\Omega\hat{\mathcal{J}}_x \qquad (2.40)$$

Thus, defining a new set of coordinates [13]

$$\hat{J}'_y(t) = +\hat{J}_y(t)\cos(\Omega t) + \hat{J}_z(t)\sin(\Omega t), \qquad (2.41)$$

$$\hat{J}'_z(t) = -\hat{J}_y(t)\sin(\Omega t) + \hat{J}_z(t)\cos(\Omega t) \qquad (2.42)$$

The equations of motion can be rewritten as

$$\hat{S}_y^{\text{out}}(t) = \hat{S}_y^{\text{in}}(t) + aS_x\left(\hat{J}'_y(t)\sin(\Omega t) + \hat{J}'_z(t)\cos(\Omega t)\right) \qquad (2.43)$$

$$\hat{S}_z^{\text{out}}(t) = \hat{S}_z^{\text{in}}(t) \qquad (2.44)$$

$$\frac{\partial}{\partial t}\hat{J}'_y(t) = aJ_x\hat{S}_z^{\text{in}}(t)\cos(\Omega t) \qquad (2.45)$$

$$\frac{\partial}{\partial t}\hat{J}'_z(t) = aJ_x\hat{S}_z^{\text{in}}(t)\sin(\Omega t) \qquad (2.46)$$

2.3 Atomic density

The atomic density in a cell can be estimated by Beer's law which relates the attenuation of linearly polarised light with the properties of the material through which the light is travelling [18] as

$$I_\nu(x) = I_0 e^{-\rho\sigma(\nu)x} \qquad (2.47)$$

Where x denotes the distance that the light crossed the absorptive medium, ρ is the density of the atom and $\sigma(\nu)$ is the absorption cross-section. Rearranging Equation 2.47 and integrating over the frequency ν leads to [17],

$$\rho = \frac{-\int \frac{I_\nu(L)}{I_0}d\nu}{L\int \sigma(\nu)d\nu} \qquad (2.48)$$

Where L is the length of the cell. The integral of the cross-section over all frequencies gives [19]

$$\int \sigma(\nu)d\nu = \pi r_e c f \qquad (2.49)$$

Where r_e is the classical electron radius, c is the speed of light, and f is the oscillator strength. Combining Equation 2.49 to Equation 2.48, we find,

$$\rho = \frac{-\int \frac{I_\nu(L)}{I_0}d\nu}{L\pi r_e c f} \qquad (2.50)$$

2.4 Faraday effect

When linear polarised light passes through matter in a longitudinal magnetic field, it experiences a rotation on its polarisation. That effect is known as the *Faraday effect* [20].

Linear polarised (π polarised) light can be decomposed as the sum of two circular polarised light with the same amplitude but with opposite rotation, clockwise (σ_+ polarised) and anti-clockwise (σ_- polarised). A wave with σ_+ polarisation couples a ground state to an excited state sublevel of magnetic number $+1$ or $\Delta m_F = 1$ [2]. On the other hand, for a wave with σ_- polarisation, the coupling is with $\Delta m_F = -1$. Thus, these two waves propagate in media with two different refractive indices, n^+ and n^- [21]. After crossing a media of length L, both waves recombine in a π polarised wave rotated by the angle [20, 21]:

$$\theta_F = \frac{\pi L}{\lambda}\left(n^+ - n^-\right) \tag{2.51}$$

where λ is the optical wavelength. This is the so-called *Faraday angle*. As seen in section 2.2, $\theta_F \propto \langle \mathcal{J}_i \rangle$ where i is the direction of the magnetic field.
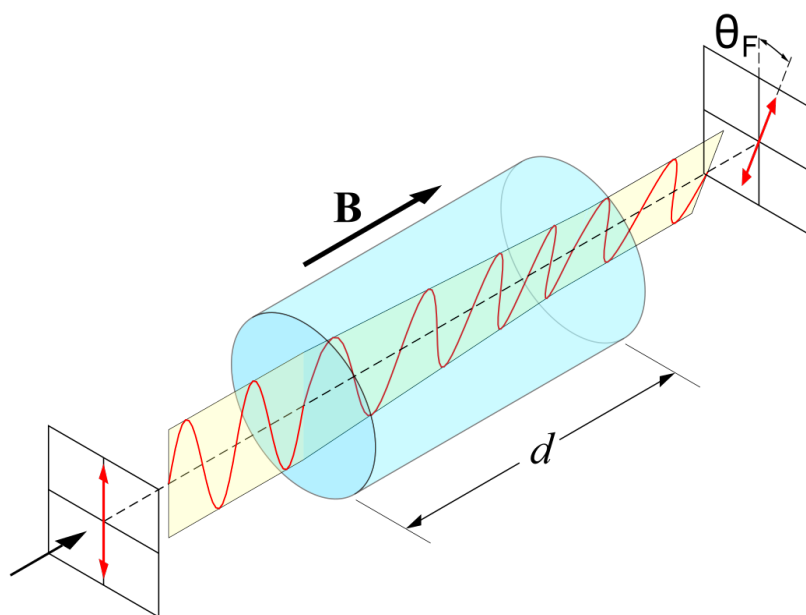

Figure 2.2.: Graphic representation of the Faraday effect. In the image, the matter under the longitudinal field is represented by the blue cylinder.
Picture extracted from [22].

---

2. Here Δm_F denotes the increment of the magnetic quantum number in a transition between two states, e.g. $6S_{1/2}\left|F = 4, m_F = 3\right\rangle \to 6P_{1/2}\left|F' = 4, m_{F'} = 4\right\rangle$

2.5 Characterisation of the spin state

In the experiments in our lab, we usually require the atomic ensemble to be prepared in a coherent spin state. To study this state, *magneto-optical resonance spectroscopy* (MORS) is used [23]. But to reduce the decoherence induced by the continuous application of pumping light, MORS is used in a pulsed regime [10].

In MORS, atoms are optically pumped along a static magnetic field, $\mathbf{B_0}$, on the x-axis, whereas they are also subjected to an RF-field, $\mathbf{B_{RF}}$, on the z-axis resonant to the atomic level splitting to modulate the transverse spin components J_y and J_z. Finally, the output signal is used to obtain the final MORS signal by doing a *fast Fourier transformation*, either manually or with a *lock-in amplifier*.

Following [17], the total macroscopic angular momentum of the atoms can be written as

$$\hat{\mathcal{J}}_x = N \sum_{m_F} m_F \hat{\sigma}_{m_F,m_F} \tag{2.52}$$

$$\hat{\mathcal{J}}_y = Re\left[N \sum_{m_F=-F}^{F-1} C(F,m_F)\hat{\sigma}_{m_F+1,m_F} \right] \tag{2.53}$$

$$\hat{\mathcal{J}}_z = Im\left[N \sum_{m_F=-F}^{F-1} C(F,m_F)\hat{\sigma}_{m_F+1,m_F} \right] \tag{2.54}$$

where $C(F,m_F) = \sqrt{F(F+1) - m_F(m_F+1)}$ and $\hat{\sigma}_{i,j} = \frac{1}{N}\sum_{k=1}^{N} |i\rangle_k \langle j|_k$ are the density operators with $i,j = -F, f+1, ..., F$ and $|i\rangle$ and $|j\rangle$ are the Zeeman magnetic sublevels in Dirac notation. We can write the Hamiltonian with the second-order correction of spins subjected to a static magnetic field $\mathbf{B_0}$ in the x-direction and RF-field $\mathbf{B_{RF}}\cos(wt+\phi)$ in the z-direction [23], as

$$\hat{H} = \sum_{m_F=-F}^{F} \hbar\omega_{m_F}\hat{\sigma}_{m_F,m_F} + \frac{g_F\mu_B}{4} \sum_{m_F=-F}^{F-1} \left(C(F,m_F)\hat{\sigma}_{m_F+1,m_F}B_{RF}e^{-i\omega t} + \text{ h.c. } \right) \tag{2.55}$$

Where the first term is the DC contribution and the second the RF. Considering all the atoms pumped to the $|4,4\rangle$ state, we only care about the decay to $m_F = 3$. Then, the equations of motion can be obtained by solving the Heisenberg equation considering the decay terms [17]. In the pulse regime, considering that the spins are highly oriented to the x-axis and hardly deviate ($\hat{\mathcal{J}}_x > \hat{\mathcal{J}}_y, \hat{\mathcal{J}}_z$), the solution of the motion equation is [23]:

$$\tilde{\sigma}_{43}(t) = \tilde{\sigma}_{43}(0)e^{(i\Delta-\Gamma/2)t} - \frac{i\chi}{i\Delta-\Gamma/2} \times [\hat{\sigma}_{44} - \hat{\sigma}_{33}]\left(1 - e^{(i\Delta-\Gamma/2)t}\right) \tag{2.56}$$

Where $\Delta = \omega - \omega_{43}$, $\chi = g_F \mu_B B_{RF} C(F,3)/4\hbar$, we introduced the slowly varying operators $\tilde{\sigma} = \hat{\sigma} e^{i\omega t}$, and Γ is the decay rate. For two neighbouring Zeeman sublevels, we have the Lorentzian response of a two-level atom, so the decay rate is equal to the line width with $\Gamma = FWHM = (\pi T_2)^{-1}$ [13].

This method can be used to compute all the density operators $\hat{\sigma}_{m_F+1,m_F}(t)$ and thus, $\hat{\mathcal{J}}_z$. Then, the outcoming signal might be expressed as the photocurrent [17]:

$$i(t) = \alpha \langle \hat{\mathcal{J}}_z \rangle = \alpha \cdot [A(t)] \tag{2.57}$$

Where $A(t)$ is the mean value of the expression in square brackets in Equation 2.54. Inserting the photocurrent $i(t)$ in a lock-in amplifier, the magneto-optical resonance signal is experimentally recorded as

$$\text{MORS}(\omega) = \alpha^2 |A(t)|^2 \tag{2.58}$$

The final spectrum has eight peaks with different heights, corresponding to each $m_F + 1 \to m_F$ transition.

Atomic orientation

The orientation parameter p represents the projection of the spin and is defined as

$$p = \frac{1}{F} \sum_{m_F=-F}^{F} m_F \langle \hat{\sigma}_{m_F,m_F} \rangle \tag{2.59}$$

The parameter will be $p = 1$ if we have all the spins in the state $m_F = 4$ and $p = 0$ if the atomic ensemble is completely unpolarised.

2.6 Spin relaxation times

Usually, in the experiments carried out in our lab, we do not pump the atoms to the $|4,4\rangle$ state continuously. Therefore, we need to characterise the lifetime of the spins of our atoms.

T_1 describes the lifetime of the longitudinal spin component $\mathcal{J}_x$; we refer to it as *depopulation time*. T_2 represents the lifetime of the transverse components $\hat{\mathcal{J}}_y$ and $\hat{\mathcal{J}}_z$; we refer to it as *decoherence time*. Assuming an exponential decay, we have [17],

$$\mathcal{J}_x(t) = \mathcal{J}_x(0) e^{-t/T_1} \tag{2.60}$$

We can define T_2 equivalently for the transverse decay. We discuss how to obtain T_1 in section 4.3 and T_2 in section 2.5.

2.6.1 Relation between T_1 and T_2

In a two-level system, we can relate the excited population decay Γ with the decoherence decay $\gamma_\perp$ with [24],

$$\gamma_\perp = \frac{\Gamma}{2} + \gamma_c \tag{2.61}$$

where γ_c models inhomogeneous decoherence decay effects such us fluctuations on the magnetic field. From [13] and [25] we know that:

$$\gamma_\perp = (\pi T_2)^{-1} \tag{2.62}$$

$$\Gamma = (\pi T_1)^{-1} \tag{2.63}$$

Adding this rate to the previous equation leads to the following relation:

$$T_2 = \frac{2\,T_1}{1 + \pi\gamma_c T_1} \tag{2.64}$$

which means that

$$T_2 \leq 2\,T_1 \tag{2.65}$$

Where $T_2 = 2\,T_1$ is absence of inhomogeneous decoherence decay effects.

Cells and Experimental setup

<div align="right">3</div>

This chapter will present an overview of the experimental setup used to characterise the vapour cells. Most of the parts covered existed before for other experiments in our lab. In the following chapters, it will be explained how all these elements and methods were used. We will describe the Cs vapour cell in section 3.1, the homogenisation of the magnetic field and the magnetic shield in section 3.2, the optical pumping technique to prepare the CSS $6S_{1/2} \left| F = 4, m_F = 4 \right\rangle$ in section 3.3 and the lasers used with a general picture of the whole experimental setup in section 3.4.

3.1 Vapour cells

The crucial part of the experiments in our lab is the vapour cell. It consists of a cylindrical glass container that contains the Cs ensemble. Each cell has a *stem* attached to the main body, where a droplet of solid Cs is stored. The whole cell is covered with an *anti-relaxation* coating called paraffin. This coating allows atoms to collide with the wall without depolarising. That effect allows a longer CSS. For a high transmission, both windows have both sides coated with an *anti-reflection* (AR) coating. The AR-coating windows have a 99.5% of transmission[3]. A scheme of the cell can be seen in Figure 3.1.

All cells have a channel inside the main volume. The length and the size of the cross-section of the channel are carefully chosen. Larger optical depth leads to stronger light-atom interaction [10]. However, large channels lead to more complex beam-channel alignments. Improper alignment might cause scattering and clipping losses. Therefore, the election of length and cross-section is a trade-off.

The new generation of cells had cells with different sizes and lengths of the channel matching the specification of each group (the exact dimensions are shown in Table 4.1). For bigger cross-sections, the channel consists of a small tube clamped to the windows, whereas for the cell that requires a microchannel, a prefabricated chip[4] had to be used.

Due to the vacuum in the cell, the solid Cs evaporates and fills the entire volume. A microhole connects the channel to the volume to allow atoms to pass. The hole size

---

3. Confirmed via measurement by Jun Jia
4. Chips were produced by VitroCom Inc.

must be small enough that the transfer of atoms in and out of the tube is negligible for experimental time scales. This allows us to assume that the atomic density in the channel is constant during the experiments. Moreover, it also allows the vapour pressure to adjust when we increase the temperature. The microhole is done by scratching one of the surfaces of the chip or the channel that is attached to the window.
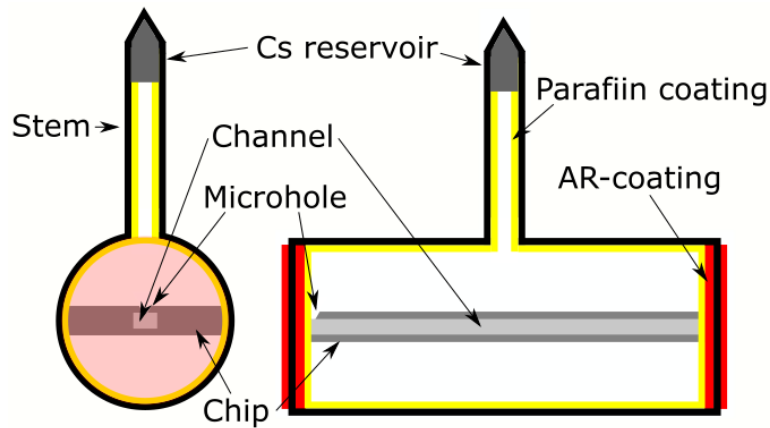

Figure 3.1.: Scheme of a microcell. The red line represents the AR-coating, whereas the yellow represents the paraffin. This figure was adapted from [26]

All the cells were manufactured by our collaborator, the Assoc. Prof. Mikhail Balabas of Saint-Petersburg State University.

3.2 Homogenisation of the magnetic field

When characterising the cells, we rely on producing homogeneous magnetic fields to split the energy levels into the Zeeman magnetic sublevels. However, fluctuations over time and inhomogeneity over the volume in the magnetic field will lead to fluctuations in the Zeeman splitting, which will introduce coherence relaxation [10]. Therefore, the relaxation times are limited by the decoherence induced by magnetic field fluctuations, especially T_2. For this reason, the cells are tested inside a magnetic shield. Inside the shield, a coil frame produces a homogeneous magnetic field. In the following subsections, both structures will be explained more in detail.

3.2.1 Magnetic shield

The magnetic shield consists of a cylindrical layer of iron and three layers of a μ-metal, a high-permeability alloy (see Figure 3.2). These layers are used to reduce the external magnetic fields progressively. The constant Earth magnetic field or the magnetic field the power-line would create are some examples of fields that can interfere with our experiments. The shield has six holes (two on every axis) to allow the laser beams to pass. Inside the shield, the coil frame creates the inner magnetic field and a plastic

holder for the cell. The holder itself is placed on a stage outside the shield that allows the alignment of the laser beam with the cell channel by lifting, lowering and rotating the cell.
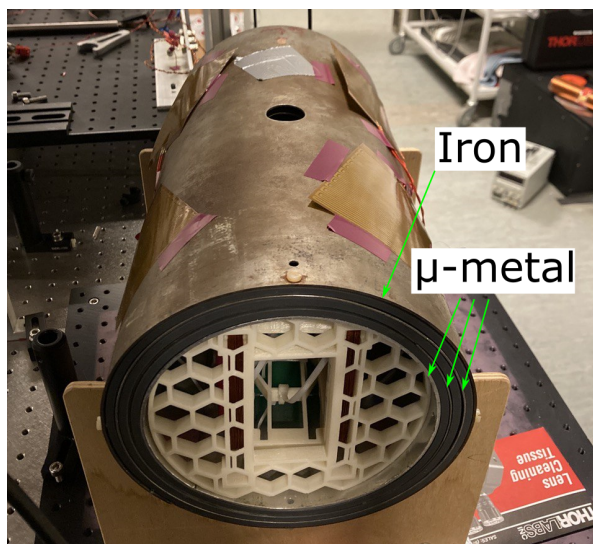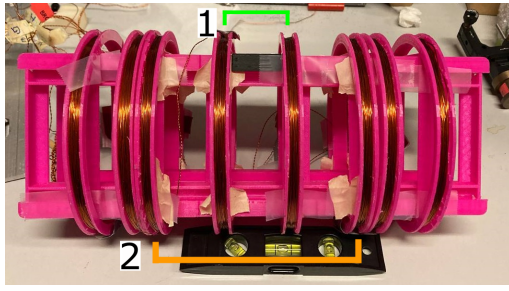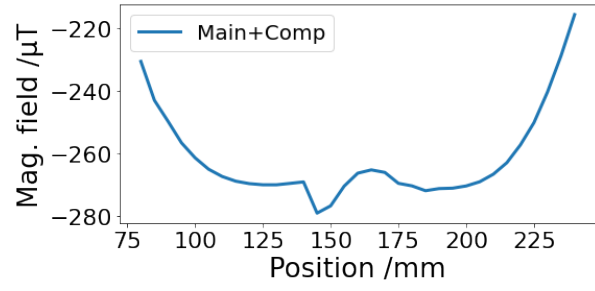
3.2.2 Coil frame and magnetic field

Our coil frame consists of a 3D printed rectangular frame with four pairs of cylindrical coils. To create a homogeneous magnetic field, we measured the field created by each pair of coils alone with a USB magnetometer[5] to then calculate an appropriate intensity ratio to compensate the curvature of the fields to improve the magnetic field homogeneity. Unfortunately, two of the pairs of coils broke. We would have to disassemble all the coils to repair them, so we proceeded with only two pairs. The second most inner pair generated a main magnetic field (see Figure 3.3 (a) orange line marked as '2') while the most inner generated a compensation magnetic field (see Figure 3.3 (a) green line marked as '1'). The compensation field was created by applying the current in the opposite direction to the compensation coils. We focused on homogenising the range of 10 cm where the cell would be placed. The current ratio was $1 : -0.58$ (the negative marks the opposite direction of the current).

We will define the axis where the magnetic field is created as the quantisation axis x.

---

5. BNO055 USB-STICK

(a) Coil frame.

(b) Total (Main + compensation) magnetic field.

Figure 3.3.: Coil frame used for the cell testing. The orange line marked as '2' indicates the main coils, while the green line marked as '1' indicates the compensation coils, which have a ratio 1:-0.58 in intensity. In Figure 3.3 (b), we can see the magnetic field. Right before the position 150 mm, we have a bump due to a re-calibration of the magnetometer. In the cell range, $[105, 205]$ mm, the STD of the magnetic field is $3.5\,\mu$T, a 1.2% normalised to the mean.

3.3 Optical pumping

For many of our experiments, we use the magnetic sublevel $6S_{1/2}\,|4,4\rangle$ as one of the ground-states levels. Therefore, to prepare the initial state, we want to put all our atoms in the magnetic sublevel $m_F = 4$. This leads to a spin polarisation along the direction of the magnetic field that we assigned as the x-axis in the previous section. The x-component of the macroscopic collective spin is then represented as $\mathcal{J}_x$.

At room temperature, atoms are equally distributed in all the Zeeman sublevels of the hyperfine manifolds $F = 3$ and $F = 4$. Therefore we use two lasers to prepare the $|4,4\rangle$ state. When atoms interact with near-resonant optical fields, transitions occur. We use these transitions to transfer all the atoms. These transitions are limited by the *selection rules*. These rules arise from the conservation of energy and momentum. Energy is conserved by matching the wavelength of the laser with the energy difference between the two levels in the transition. From the conservation of the momentum, we get a group of constraints on the difference of the quantum numbers between the two levels in the transition [11].

$$\Delta L = \pm 1 \tag{3.1}$$

$$\Delta S = 0 \tag{3.2}$$

$$\Delta J = 0, \pm 1 \tag{3.3}$$

$$\Delta F = 0, \pm 1 \tag{3.4}$$

$$\Delta m_F = \text{depends on the polarisation of the light} \tag{3.5}$$

We want to drive the atoms to the $|4, 4\rangle$ state. Therefore, we use right-handed circularly polarised light, σ_+, with an $\Delta m_F = +1$. The atom can decay with spontaneous emission with $\Delta m_F = \pm 1, 0$. That means that the quantum number m_F never decreases and, on average, increases. If an atom reaches $m_F = 4$, it will not couple to the light since the selection rules don't allow any transition. At this point, the atoms will not move further. We call this state a *dark state*. This is called *optical pumping*. Occasionally, atoms may decay to the hyperfine level $F = 3$. In that case, we need to *repump* the atoms to the $F = 4$ state. Both optical pumping and repumping are schematically shown in Figure 3.4.

In our experiment, we pump with a laser tuned to the $F = 4 \rightarrow F' = 4$ transition of the D_1-line ($6S_{1/2} \rightarrow 6P_{1/2}$). And we repump with a laser tuned to the $F = 3 \rightarrow F' = 2, 3$ crossover transition of the D_2-line ($6S_{1/2} \rightarrow 6P_{3/2}$).
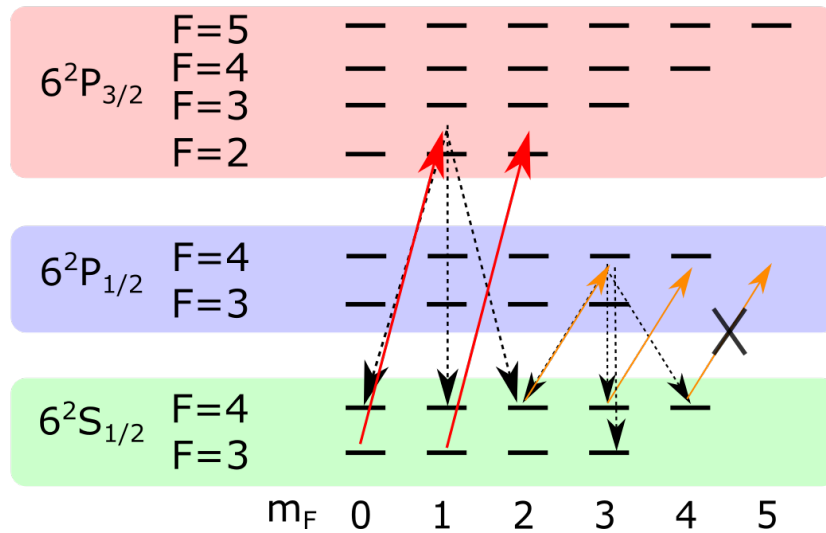

Figure 3.4.: Representation of the optical pumping (orange arrows) and repumping (red arrows) in the Cs' level structure. The crossed orange arrow marks the dark state $|4, 4\rangle$ where are remain.

3.4 Experimental setup

For both absorption and T1 measurements, only laser beams propagating along the cell channel are required. All the lasers we used went through the cell in the same direction. As discussed in the previous section, to pump the atoms to the $|4, 4\rangle$ state, we used a laser with a wavelength of $\lambda = 895\,\text{nm}$ (D_1 line). The laser is a TOPTICA *External Cavity Diode Lasers* (ECDL)[6]. To repump the atoms from the $F = 3$ manifold, we used a laser tune to $\lambda = 852\,\text{nm}$ (D_2 line). The laser is a TOPTICA ECDL[7]. To read

6. TOPTICA DL 100 diode laser
7. TOPTICA DL 100 diode laser

out the state of the atoms, we used a third laser called *probe*. The probe laser is a TOPTICA ECDL[8], and it is blue detuned $\Delta \sim 2$ GHz with an *Electro-Optical Modulator* (EOM) from the croosover transition $F = 4 \rightarrow F' = 4, 5$ of the D_2-line ($\lambda = 852$ nm). The lasers are locked using Doppler-free spectroscopy [8, 10].

To optimise the optical pumping, we ensured that the polarisation of both lasers was circular using a half-wave plate (HWP) and a quarter-wave plate (QWP). For the probe, we wanted linear polarisation obtained with a HWP and a QWP. All three lasers were later overlapped with beam splitters (BS). Then, the lasers cross the cell through the channel, and we read out its response with a detector.

For the T_1 measurement, we used all three lasers and a balanced photodetector (BPD) to do the homodyne detection (green areas in Figure 3.5). But for the absorption measurement, to avoid broadening and depumping effects, we had to use low powers. To get a good signal to noise ratio, we required an avalanche photodiode (APD). To ensure low powers, we placed some attenuators in the path. Besides that, we used a Mach-Zender interferometer (MZI) to correct the non-linearity of the probe scan of the frequency (blue areas in Figure 3.5). Both experiments and setups are explained in more detail in the next Chapter 4.

A general overview of the experimental setup is shown in Figure 3.5.
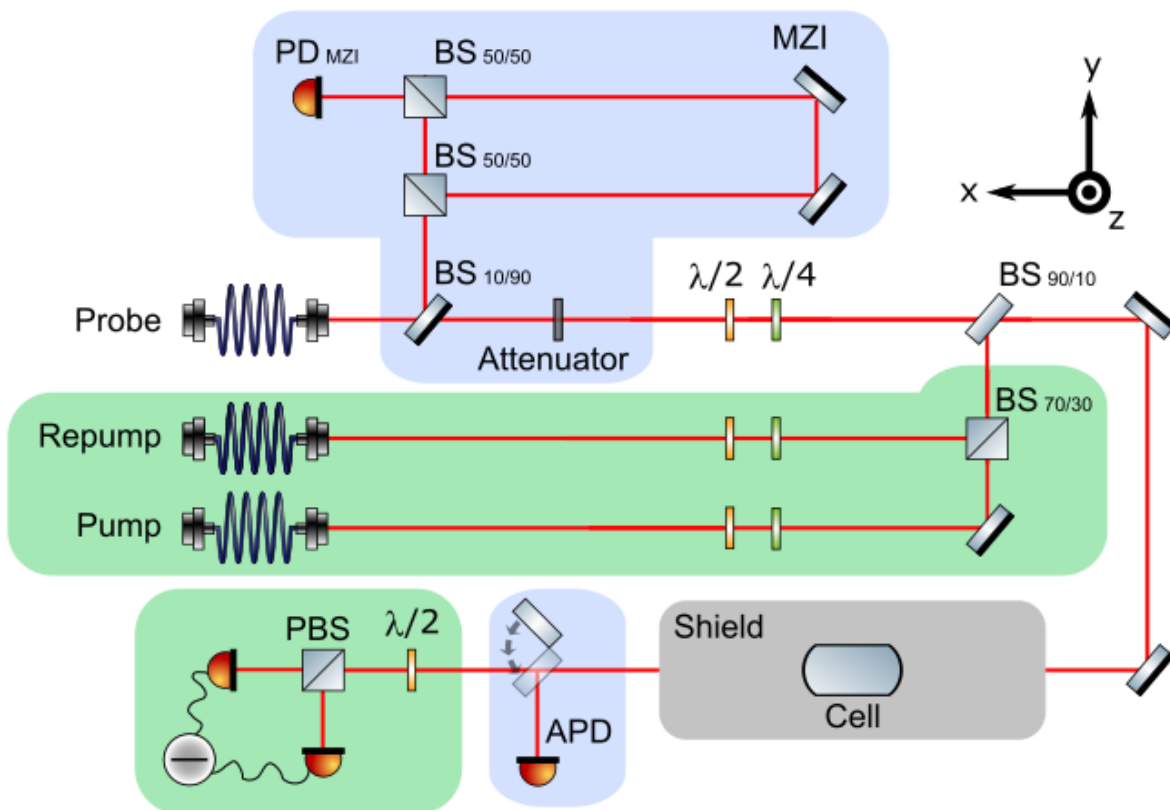
---

8. TOPTICA DL Pro diode laser

Figure 3.5.: Experimental setup used for the characterisation of the cells. Green areas were used for the T_1 measurement, whereas the blues were used for the absorption measurement. Areas without a background colour were used in both experiments. This figure was created using A. Frazen's *svg component library*.

Cell characterisation

<div style="text-align: right; font-size: 3em;">4</div>

NOTE: The following test and results of T_2 measurement were provided by Jun Jia and Ryan Yde. For transmission, absorption and T_1 measurement, the test and results were obtained in collaboration with Rebecca Schmieg.

Vapour cells are a crucial element in our experiments. Therefore they have to be subjected to various tests. Namely:

- A *transmission* measurement: allows us to know how well light travels along the cell and how much light we lose.

- An *absorption* measurement: allows us to determine the atomic density of the atoms ins the channel.

- A **T**$_1$ measurement: the spin depopulation time allows us to determine the decay of the longitudinal spin component $\hat{\mathcal{J}}_x$.

- A **T**$_2$ measurement: the spin decoherence time allows us to determine the decay of the transverse spin components $\hat{\mathcal{J}}_y$ and $\hat{\mathcal{J}}_z$.

For all the tests, the waists of the beams were adjusted to fit the channel[9]. A beam too big would lead to clipping and scattering losses. And a beam too small might not reflect the characteristics studied adequately.

4.1   Transmission

For the transmission measurement, we measured the intensity of a laser before and after placing a cell, usually the probe. A ray diagram of this experiment is shown in Figure 4.1. Cells are aligned to the beam to maximise the transmission. The waist of the beam is adjusted too to avoid scattering and clipping effects.

---

9. All the beam's waists were checked during the thesis using the BP209-VIS/M waistmeter from Thorlabs [27]. It allowed us to determine the waist of a beam in two perpendicular directions and record bitmap images of the profiles. In addition, the interface of the waistmeter permitted us to compare the longitudinal and transversal projection of the beam with a Gaussian and compare how close they were.
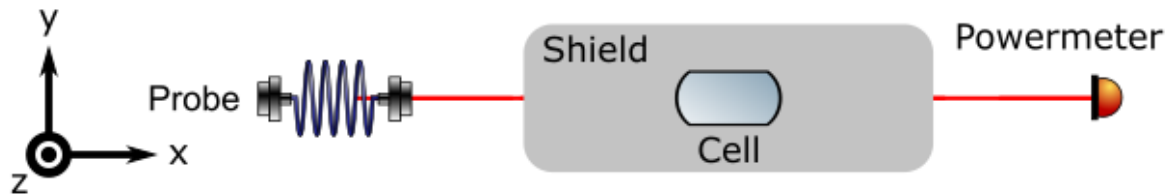
Figure 4.1.: Ray diagram of the transmission measurement. Power was measured with and without the cell to determine the transmission of each cell. Usually, we use the probe to state the total transmission.
This figure was created using A. Frazen's *svg component library*.

Windows with anti-reflective coating have a 99.5% of transmission. Thus, we would expect a transmission of 99%. However, the maximum transmission we obtained through a cell was 96.7% (see Table 4.1). A further study revealed that the windows reflected nearly 1.5% for different bare and filled cells [25]. This would indicate that this reflection was not caused by the coating but by defects in the windows produced during the glass-blowing. Defects such as cracks, cuts, and additional curvature added to the windows during the cell fabrication process. A tilt, a bend or a twist in the channel also introduces losses (see Figure 4.2). But, while the tilt can be compensated in the aligning process, a bend or a twist have more complex ways to overcome. When the performance was poor due to the coating, re-curing the cells usually helps. To re-cure procedure consists of creating a temperature gradient between the cell and the stem for a long time. This is accomplished by warming the cells in an oven at 60-70 degrees for 12 hours with the stem covered with wet cotton [25].
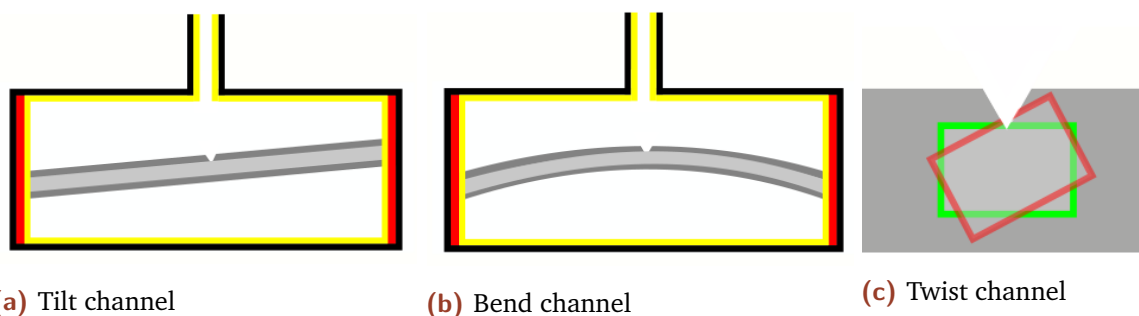

(a) Tilt channel   **(b)** Bend channel   **(c)** Twist channel

Figure 4.2.: Cell defects caused by imperfections in the channel. In Figure 4.2 (c), the green square represents the orientation of the channel in the input and the red square in the output.

4.2 Atomic density

The absorption measurement is used to determine the atomic density. This section will explain the method used to determine the atomic density of our new cells, including the experimental setup, the experiment, and the analysis.

4.2.1 Experimental setup

For the absorption measurement, the probe laser was used to scan the transitions over the two manifolds of the hyperfine levels of the grounds state $6S_{1/2}$ ($F = 3$ and $F = 4$) to the excited state $6P_{1/2}$ (D_2 line). We used low power (range within 20 nW and 1 μW) to avoid broadening and population redistribution. In image Figure 4.4, we can see an asymmetry in the absorption dips for high powers that disappear for low powers. Also, we used a slow scan of 10 Hz to avoid a non-equilibrium population between the ground state manifolds. To correct the non-linearity of the frequency scan, we used an asymmetric MZI with a path difference of 2.58 m. The absorption signal was recorded with an APD while the MZI with a variable gain photodetector (PD), as shown in Figure 4.3.
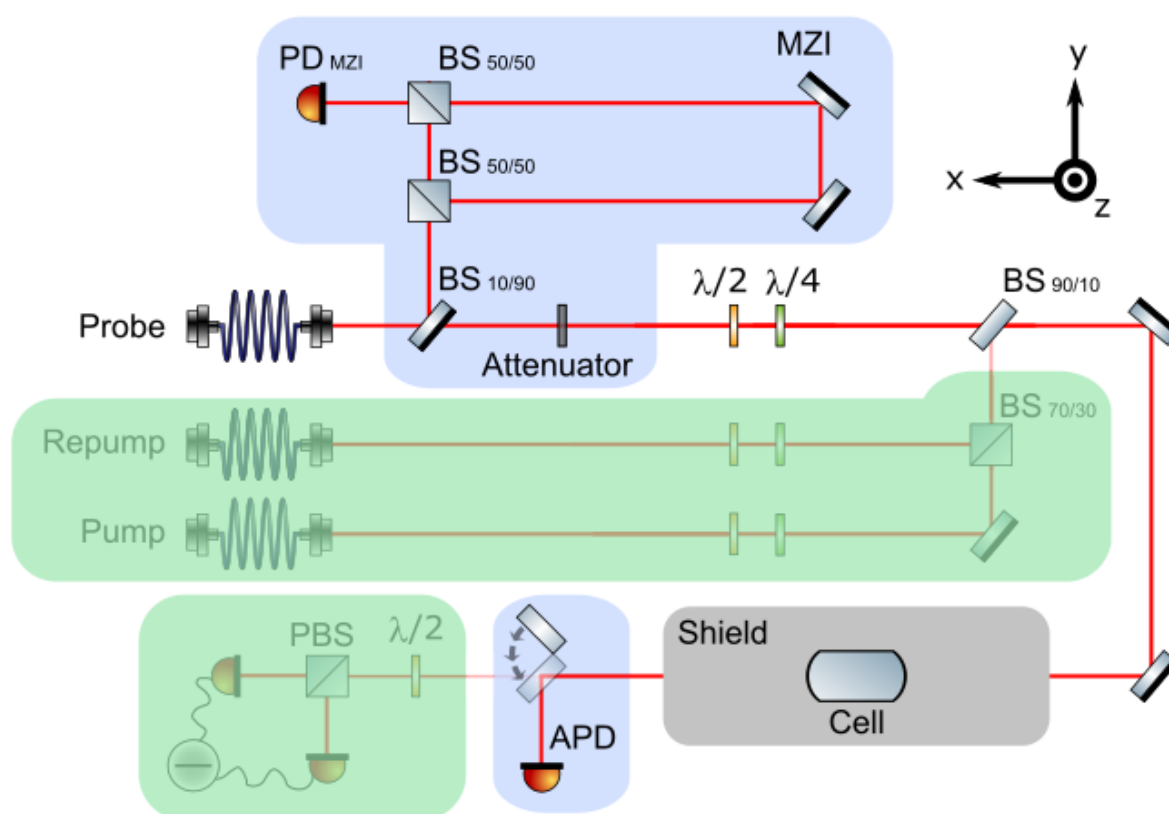

Figure 4.3.: Absorption laser diagram. The probe laser is detected with APD, whereas the MZI records a signal simultaneously to correct the non-linearity of the frequency scan of the probe.
This figure was created using A. Frazen's *svg component library*.

4.2.2 Absorption measurement

As mentioned before in section 4.2.1, to correct the non-linearity of the scan, we recorded the signal from the MZI and the absorption spectrum at the same time. In Figure 4.4, we can see that the power of the laser depends on the position of the scan. Hence, we did a linear fit to obtain the power dependence of the scan. With this dependence, we could normalise the signal.
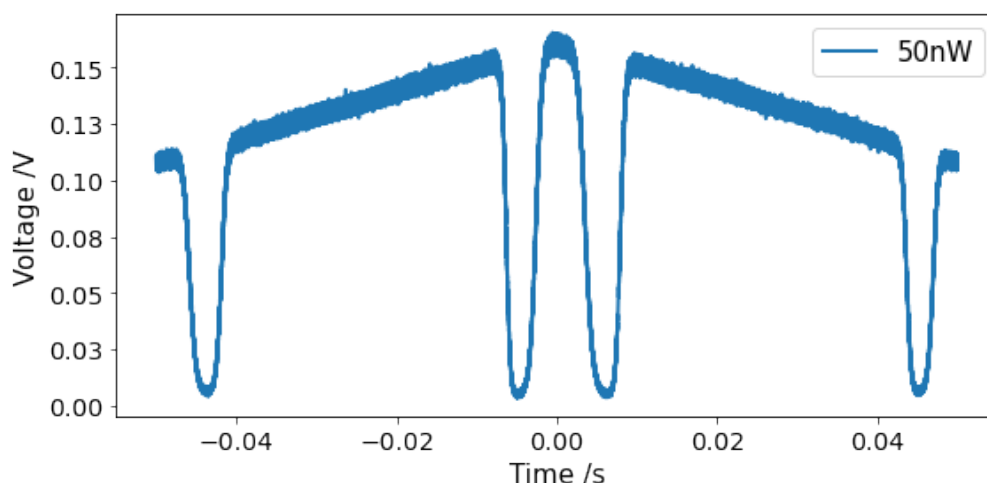
(a) Absorption spectrum probing with 50 nW.
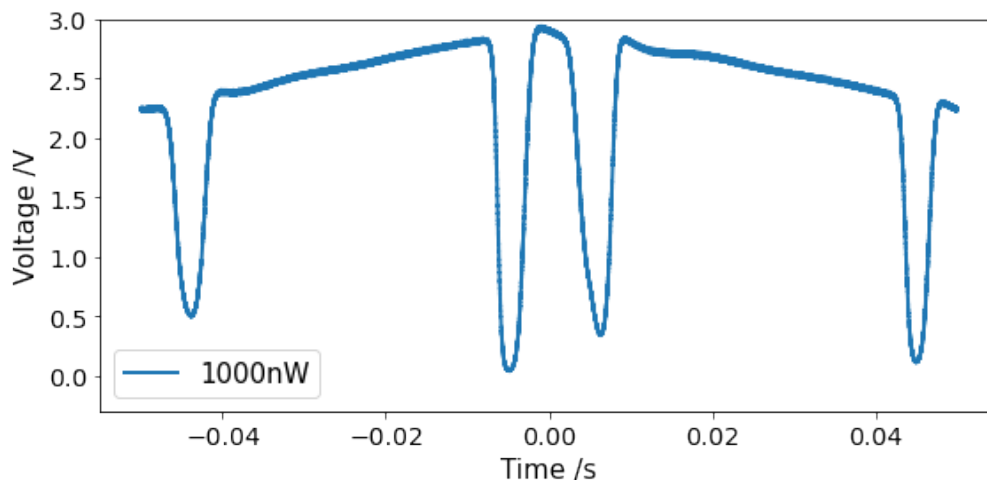
(b) Absorption spectrum probing with 1000 nW.

Figure 4.4.: Absorption spectrum for 50 nW and 1000 nW. In Figure 4.4b (b), it can be clearly seen an asymmetry in the absorption dips for high powers.

For considerable optical depth, the absorption of the signal can drop to intensities near-zero (full absorption). As the absorption spectrum is limited by the optical depth, using the raw data in Equation 2.50 can lead to inaccurate results. To avoid this problem, we used a model of the absorption spectrum of the D_2 line to fit the data.

4.2.2.1 Absorption spectrum Model

NOTE: The absorption spectrum model used to fit the data including the program used for the analysis was obtained from Schmeig 'Coherent dynamics of atomic vapours' [28].

According to the selection rule Equation 3.4,

$$\Delta F = 0, \pm 1 \tag{4.1}$$

If we scan over the two manifolds $F = 3$ and $F = 4$ of the ground state, only six transitions are allowed:

$$F = 3 \rightarrow F' = 2, 3, 4 \tag{4.2}$$

$$F = 4 \rightarrow F' = 3, 4, 5 \tag{4.3}$$

And since we are probing with a linear polarisation light $\Delta m_F = 0$. As a consequence of the splitting of the hyperfine levels, each transition has different resonance frequencies. Moreover, each transition between different Zeeman sublevels has different strengths proportional to the Clebsh-Gordan coefficients [28].
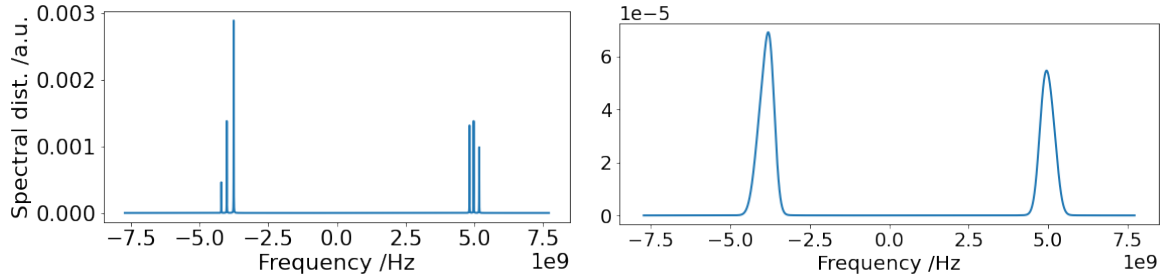
Ideally, with all these considerations along with assuming thermal equilibrium and homogeneous broadening, the absorption spectrum is obtained as a superposition of six Lorentzian spectral components [28]:

$$S(\nu) = \sum_{F,F'} \sum_{m_F} A_{FF'}^{m_F} \frac{\gamma/2}{\left(\nu - \nu_0^{FF'}\right)^2 - (\gamma/2)^2} \tag{4.4}$$

Where the Lorentzians (obtained from [24]) are located in the resonant frequencies of the D_2 line $\nu_0^{FF'}$ with width of the decay rate γ. $A_{FF'}^{m_F}$ is a normalisation factor that includes the Clebsch-Gordan coefficients. The sums are over all the possible transitions described before.

In reality, each atom has different velocities distributed according to the Maxwell-Boltzmann distribution. These different velocities lead to distinct Doppler shifts, which lead to Gaussian line shapes [24]. We take into account these effects by convolving the Lorentzians of Equation 4.4 with a Gaussian velocity distribution [24, 28], and the resulting line shape is the Voigt profile [18]. For our case [28]:

$$S(\nu) = \sum_{F,F'} \sum_{m_F} A_{FF'}^{m_F} \int_0^\infty d\nu \frac{\gamma/2}{\left(\nu - \nu_0^{FF'}\right)^2 - (\gamma/2)^2} \cdot c_D \exp\left(4\ln 2 \left(\frac{\nu_0^{FF'} - \nu_D}{\Delta \nu_D}\right)\right) \tag{4.5}$$

(a) Spectral distribution of the six possible transitions. **(b)** Convolution of the six transitions into two overlapped peaks.

Figure 4.5.: Absorption model design to fit the spectrum obtained. In Figure 4.5 (a), we can see the spectral distribution of the six possible transitions $F = 3 \rightarrow F' = 2, 3, 4$ and $F = 3 \rightarrow F' = 2, 3, 4$. In Figure 4.5 (b), we can see the two overlapped peaks resulting of the Doppler broadening caused by the convolution of the Lorentzian spectral components with the Gaussian velocity distribution.
Figures obtained with the code provided in [28].

Where c_D incorporates the normalisation factors for the Gaussian distribution and $\Delta\nu_D$ is the Doppler width. The convolution in the Voigt profile allows us to represent the Doppler broadening in the spectrum, which leads to two overlapping peaks in the absorption spectrum. In the absorption spectrum in Figure 4.5 (b), we can see the two peaks corresponding to the overlapping absorption peaks.

As mentioned before in section 2.3, light is absorbed when it passes through an atomic medium following an exponential relation.

$$I_\nu (x) = I_0 e^{-\alpha(\nu)x} \tag{4.6}$$

Where the absorption coefficient $\alpha(\nu)$ is directly related to the spectral distribution stated in Equation 4.5 [24]. Thus, the model used to fit the absorption data is the one described in [25]:

$$\frac{I_\nu(x)}{I_0} = \exp\left(c_1 \cdot S\left((\nu - c_2) \cdot c_3\right)\right) \tag{4.7}$$

Where the fitting parameters are c_1 an overall scaling factor, c_2 the centre of the spectrum, c_3 a correction to our frequency scaling. Once we have the fit we can compute the atomic density with Equation 2.50 with $r_e = 2.817 \cdot 10^{-15}$ m [29] and $f = 0.7164$ [12]. From the absorption spectrum of the cell $O15$, Figure 4.6 we obtained an atomic density of:

$$\rho = (2.9 \pm 0.1) \cdot 10^{16} \text{ m}^{-3} \tag{4.8}$$

The error in these measurements is the statistical error obtained from various samples of the absorption measurement and for different powers.
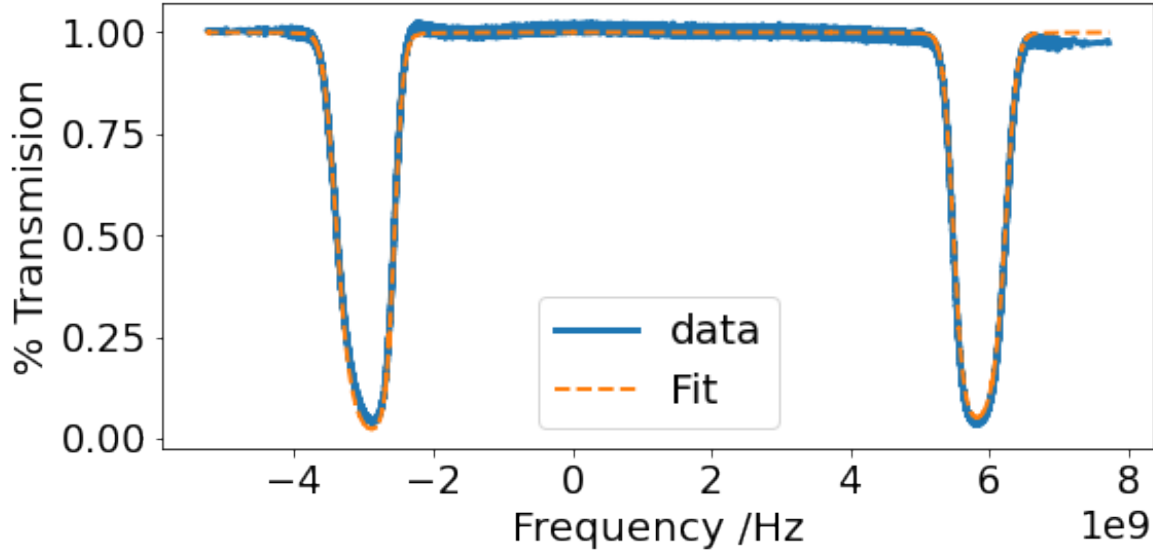
Figure 4.6.: Absorption measurement (blue line) fitted with the convolution model (orange dashed lines). From this fit, the atomic density can be obtained with Equation 2.50.

The results for this measurement for the other cells tested are shown in Table 4.1.

4.3 Depopulation time - T_1

As mentioned before in section 2.6, $\langle \mathcal{J}_x \rangle$ decay exponentially with T_1, proportional to the Faraday angle θ_F. Therefore, measuring the decay of θ_F allows us to obtain the T_1 value. This section will explain the methodology used to determine the T_1 of our new cells, including the experimental setup, the experiment and the analysis.

4.3.1 Experimental setup

To determine T_1, we combined a pulse to optically pump the atoms to the $|4, 4\rangle$ state with a second pulse to read out the decay of the Faraday angle. We used AOMs and a function generator to generate the pulses. We can recall from section 2.4 that the polarisation of linearly polarised light rotates as it passes through an atomic sample polarised in the direction of the propagation. The beam diagram of this measurement can be found in FIG. 4.7.

The sequence used was:

1. $500\,\mathrm{ms}$ of optical pumping (long enough to prepare the atomic ensemble to the $|4, 4\rangle$ state.)

2. $100\,\mathrm{ns}$ of delay to avoid overshooting responses of the detector

3. Probing (multiple T_1 times)

To optimise the initial state, we had to ensure that the polarisation of the optical pumping was circular with a QWP and a HWP. For the detection, we used a BPD.
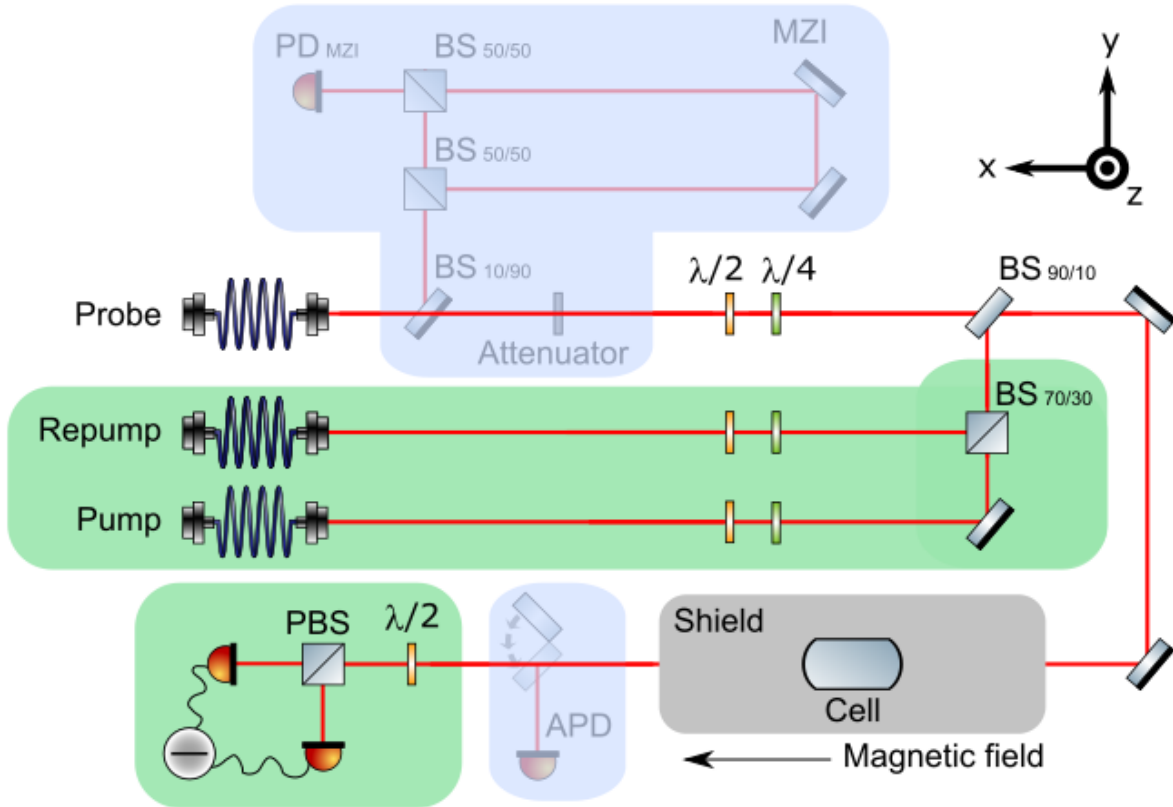

Figure 4.7.: Ray diagram of the experimental setup used to compute T_1. The polarisation of the beams (circular for pump and repump and linear for the probe) is controlled with HWP and QWP. The detection of the Faraday decay is done with a BPD. This figure was created using A. Frazen's *svg component library*.

4.3.2 Balanced detection

The electric field of a linear polarised wave travelling along the propagation x-axis can be written as the superposition of two perpendicular linear polarised waves oscillating in the $y-$ and z-axis [30]. For a linear polarised wave rotated by an angle ϕ from the horizontal direction, we can write the electric field as

$$\mathbf{E} = E_c \cos{(\phi)}\, \mathbf{e}_y + E_c \sin{(\phi)}\, \mathbf{e}_z \qquad (4.9)$$

Where $E_c = E_0 \cos{(kx - \omega t)}$ is the so-called *complex amplitude* which describes the electric field of both orthogonal waves propagating along the x-axis. E_0 is the amplitude of the field, and $\mathbf{e}_i$ denotes the vector component in the direction i. If we split both

components in a polarising beam splitter (PBS)[10] and measure their intensity with two PDs, we will have

$$I_1 = |E_y|^2 = E_c^2 \cos^2(\phi) \tag{4.10}$$

$$I_2 = |E_z|^2 = E_c^2 \sin^2(\phi) \tag{4.11}$$

From these equations, we can see that for a $\phi = \pi/4$ angle, both intensities are the same. This polarisation can be obtained with a HWP. When both detectors of the PD receive the same intensity, we call the signal *balanced*, and its light field can be expressed as

$$\mathbf{E} = E_c \cos\left(\frac{\pi}{4}\right) \mathbf{e}_y + E_c \sin\left(\frac{\pi}{4}\right) \mathbf{e}_z \tag{4.12}$$

For the light suffers a rotation, for example, due to the Faraday effect both, components will gain a phase of θ_F, and its electrical field would be,

$$\mathbf{E} = E_c \cos\left(\frac{\pi}{4} + \theta_F\right) \mathbf{e}_y + E_c \sin\left(\frac{\pi}{4} + \theta_F\right) \mathbf{e}_z \tag{4.13}$$

And the intensities,

$$I_1 = E_c^2 \cos^2\left(\frac{\pi}{4} + \theta_F\right) \tag{4.14}$$

$$I_2 = E_c^2 \sin^2\left(\frac{\pi}{4} + \theta_F\right) \tag{4.15}$$

Following [17], we can obtain the Faraday angle θ_F with some algebra:

$$I_1 - I_2 = E_c^2 \left[\cos^2\left(\frac{\pi}{4} + \theta_F\right) - \sin^2\left(\frac{\pi}{4} + \theta_F\right)\right]$$
$$= E_c^2 \cos\left(2\left(\frac{\pi}{4} + \theta_F\right)\right) = E_c^2 \sin(2\theta_F) \tag{4.16}$$

$$I_1 + I_2 = E_c^2 \left(\cos^2\left(\frac{\pi}{4} + \theta_F\right) + \sin^2\left(\frac{\pi}{4} + \theta_F\right)\right) = E_c^2 \tag{4.17}$$

Combining the last two expressions we find

$$\theta_F = \frac{1}{2} \arcsin\left(\frac{I_1 - I_2}{I_1 + I_2}\right) \tag{4.18}$$

From this expression, we can find the value of the Faraday rotation with the intensities of the BPD. Measuring the decay of θ_F until the signal is balanced again allows us to obtain the value of T_1.

---

10. Polarised beam splitters split an incident beam into two beams of different linear polarisation.

4.3.3 Methods and analysis

First, with the optical pumping blocked, we balanced the BPD with a HWP, so both detectors received the same intensity. Unblocking the optical pumping led to a rotation of the probe. This rotation varied the intensities that each detector of the BPD received. This effect was translated into a sudden increase in the signal. When atoms decay $|4, 4\rangle$, the matter aligned to the magnetic field that produced the Faraday effect decreased so did the rotation caused to the light. This decrease continued until the thermal equilibrium was reached again and the BPD signal was balanced again. This was translated to a decay signal proportional to the length of the macroscopic spin.

From Equation 2.60, we know that the macroscopic spin decays like an exponential. Thus, we can obtain T_1 at a specific power by fitting the signal with an exponential function with an offset like:

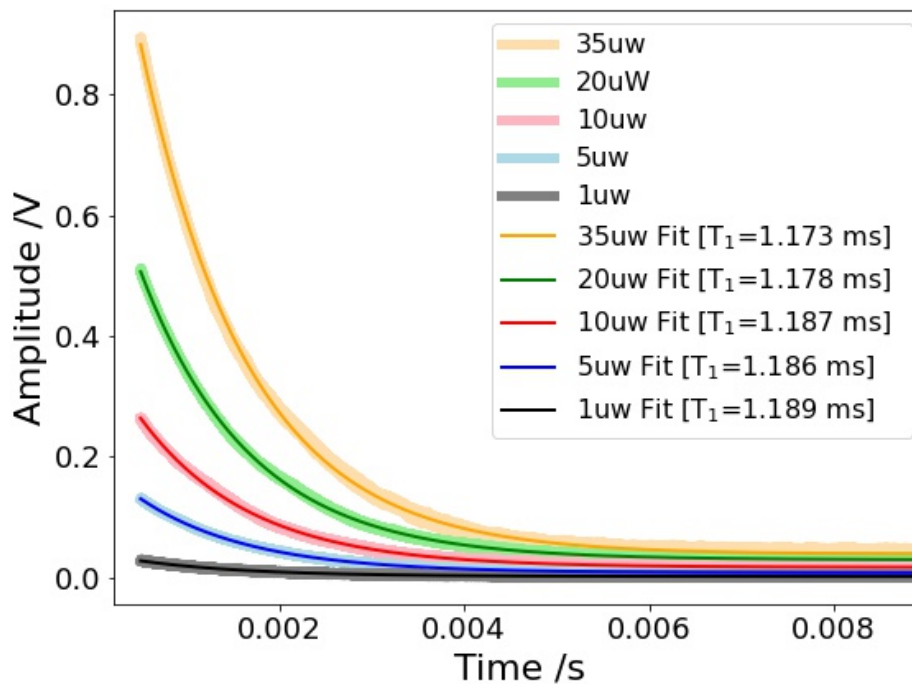$$f(t) = c_1 \cdot \exp\left(-\frac{t}{T_1}\right) + c_2 \tag{4.19}$$

Figure 4.8.: Decay signal obtained at the BPD at different powers fitted with the exponential described in Equation 4.19. These results correspond the cell $O16$.

As we want the depopulation time in the dark (no laser applied), we repeated the measurement for different values of the probe power. Then we fitted the result to extrapolate the T_1 value in the dark, as shown in Figure 4.9.

For the case shown in the Figure 4.8 and Figure 4.9, the cell $O16$, the T_1 computed was

$$T_1 = 1.19 \pm 0.02 \text{ ms} \tag{4.20}$$

The error in these measurements is the statistical error obtained through the fit.

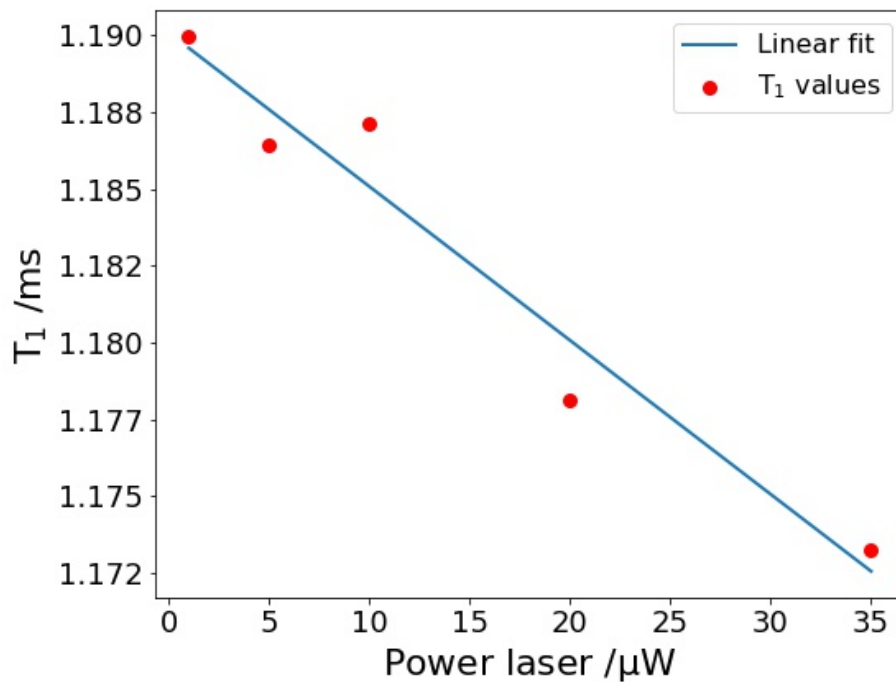The results for this measurement for the other cells tested are shown in Table 4.1.

Figure 4.9.: T_1 as a function of the probe power. From these measurements we can extrapolate the T_1 in the dark. These results correspond the cell $O16$.

4.4 Results

In the following Table 4.1, there are the results of the before-mentioned tests.

Table 4.1.: Results of the tests mentioned in sections section 4.1, section 4.2 and section 4.3. This table is extracted from [25].

Cell	Size /mm^3	%Trans.	Density ρ /10^{16}/m^{-3}[11]	T$_1$ /ms[12]	T$_2$ /ms[13]
O1	40x1x1	94.7	(2.33 ± 0.01)	5.7 ± 0.1	
O2	40x1x1	96.2	no atoms	no atoms	
O3	40x1x1	96.4	(2.51 ± 0.00)	4.7 ± 0.1	
O4	40x1x1	96.0	(2.31 ± 0.09)	2.5 ± 0.1	
O11	40x1x1	95.8	(2.70 ± 0.00)	2.8 ± 0.1	
O22	40x1x1	94.9	(2.9 ± 0.3)	5.9 ± 0.1	
O5	60x1x1	96.1	(4.04 ± 0.07)	2.4 ± 0.1	
O6	60x1x1	87.6	no atoms	no atoms	
O7	80x2x2	96.7	(2.65 ± 0.04)	6.4	5.9
O8	80x2x2	96.3	(2.95 ± 0.11)	9.1	10
O12	80x2x2	95.2	(2.77 ± 0.09)	4.5[14]	7.8
O13	80x2x2	95.4	(2.39 ± 0.15)	5.9	5.8
O15	80x2x2	95.8	(2.9 ± 0.1)	7.2 ± 0.1	9
O9	25x0.5x0.5	94.9	(0.81 ± 0.02)	1.05 ± 0.02	
O10	25x0.5x0.5	71		0.4 ± 0.01[15]	
O16	25x0.5x0.5	91.0	(2.36 ± 0.01)	1.19 ± 0.02	
O14	80x(4π)	93.5		16	
O17	80x(4π)	96.2	(3.7 ± 0.1)	20	
O18	80x(4π)	96.4	(3.54 ± 0.02)	6.5[16]	
O19	80x3x3	94.8	(3.78 ± 0.02)	11.5	
O20	80x3x3				
O21	80x3x3	95.3	(4.8 ± 0.4)	7	

---

11. [table] These measurements were done in collaboration with Rebecca Schmieg.
12. [table] These measurements were done in collaboration with Rebecca Schmieg.
13. [table] These numbers were provided by Jun Jia and Ryan Yde.
14. [table] This was after re-curing, before re-curing this cell, it had dropped to 1 ms. Comparison between both times, therefore maybe not reliable.
15. [table] This result was obtained after re-curing three times. Before, the transmission was even lower.
16. [table] This result was obtained after re-curing. Before re-curing, it was 8.5 ms. The only example where re-curing made it worse.

4.4.1 T_1 vs. T_2

In subsection 2.6.1, we determined that the relation between T_1 and T_2 is $T_2 \leq 2T_1$ (see Equation 2.65). Hence, we determined the relation that our cells exhibit by fitting a linear fit to the relation between both times. In Figure 4.10, we compare the relation of T_1 with T_2 for the new cells. L3 is an old cell we used to test the setup before we had the new cells.
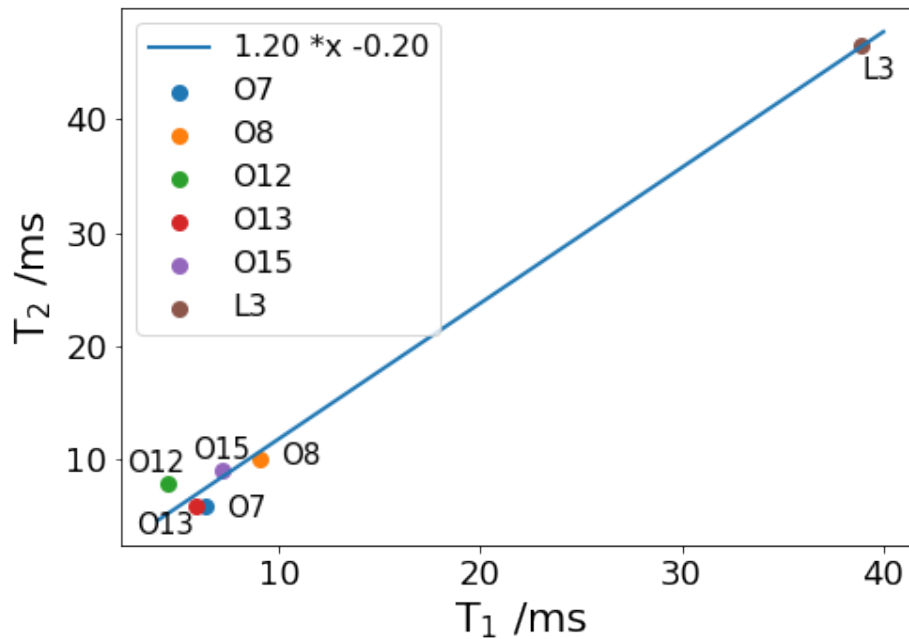

Figure 4.10.: T_2 as a function of T_1. The new cells were compared to one old cell to check if their behaviour matched. The blue line is a linear fit to extrapolate more precisely the relation between both times.

The parameters obtained from the fit were:

$$a = 1.16 \pm 0.04 \qquad (4.21)$$

$$b = 0.08 \pm 0.04 \qquad (4.22)$$

This would mean that for our cells, we can expect that,

$$T_2 \approx 1.16T_1 \qquad (4.23)$$

4.5 Discussion

As previously mentioned, the vapour cells are a crucial part of our experiments. Therefore, it is essential to know its features. In this part of the thesis, we have covered

the methods and results for cell characterisation. More concretely, we measured the transmission of light through the cell, the absorption of light to determine the atomic density and the Faraday rotation, which allows us to obtain the depopulation time T_1 measurement[17].

Discarded cells

Of all the cells tested, four cells performed considerably worse.

- O2 had no atoms inside, so we did not get any signal, so it was discarded.

- O6 had no atoms inside, so we did not get any signal. Besides, its channel was twisted. It was discarded.

- O10 after had a considerably low transmission, only 71% after being re-cured three times. Thus, it was discarded.

- O20 had the channel loose. It made it complicated to align and measure. Therefore, it was discarded as well.

The test result will be discussed without taking these cells into account.

Transmission

For the rest of the cells, the majority had a transmission between 94.7% and 96.7%. The outliers are O9 (91.0 %) and O14 (93.5%).

We would generally expect up to a 1.5% loss per window (including the 0.5% of the AR-coating). Therefore, the rest of the reduction in the transmission comes from additional defects introduced to the cell in the glass-blowing process. These defects are for example the bending or twisting of the channel.

We do not know exactly where the transmission loss comes from. However, there are some solutions to consider. To solve the glass-blowing complications in the channel, we could use a solid volume and drill a channel of the desired size on it. Thus, it would not bend, twist or get loose. For the complications on the window, a new shape for the windows was defined in [25]. The new form consists of a cylindrical window with a wedged shape, as shown in Figure 4.11. With this new window in the glass-blowing process, it would only be needed to heat the outer part of the window. Therefore the central part would be less affected.

---

17. Recall the decoherence time T_2 measurements were done by Jun Jian and Ryan Yde.
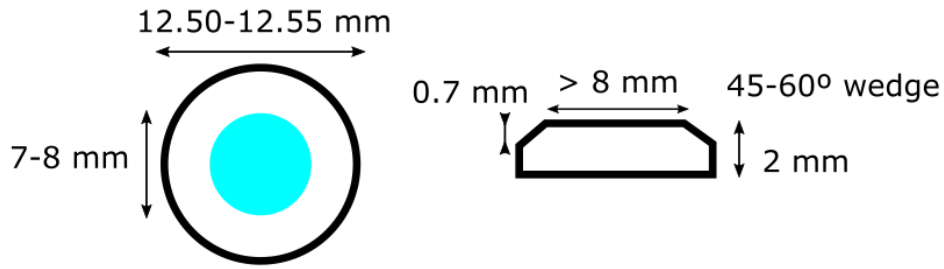
Figure 4.11.: Possible new design for the windows with a wedged shape and AR-coating only in the centre.
Image extracted from [25].

Atomic density

For the atomic density, we see that for the cells that have atoms in the channel, all the densities are of the same order of magnitude.

$$\rho \sim 10^{16} \text{ m}^{-3} \tag{4.24}$$

at room-temperature. This value agrees with the values of old cells used in the experiments.

With this order of magnitude, the smallest cells (25x0.5x0.5) will have $N_a \sim 10^7$ Cs atoms in the channel and the biggest (80x4π), $N_a \sim 10^{10}$.

T_1 and T_2

T_2 is more sensitive to the magnetic field inhomogeneity and usually is the one that limits our experiments, so usually, we are more interested in T_2. But, since for measuring T_1, we measure the decay of the Faraday angle, we do not need a perfect initial state which makes T_1 easier to measure experimentally and more practical to obtain feedback. Moreover, with Equation 2.65, we can define an upper bound for T_2.

However, we are still interested in the value of T_2. Since there was an experimental setup available for cells of size $80 \times 2 \times 2$, T_2 was experimentally determined. With the relaxation times of these cells, we extrapolated the relation between the two times to be

$$T_2 \approx 1.16 T_1 \tag{4.25}$$

But, as the magnetic field produced by the coil frames used in the different experiments in the lab is not the same, we have to be aware that this relation might only be an indicator, and it might not be accurate. It should be used as an estimation for T_2.

It has also been observed that the re-curing process usually increases (or recovers) the T_1 and T_2 values. For example, in the case of O12, it had degraded between the T_2 (7.8 ms) and T_1 (1 ms) measurements. With the values obtained, the relation in Equation 2.65 was not fulfilled. After re-curing, T_1 increased to 4.5 ms, fulfilling the relation. Only in the case of O18 T_1 got worse (8.5 ms $\rightarrow$ 6.5 ms).

The cells proposed for the single-photon experiments are the ones with $80\,\text{mm}$ length and $2 \times 2\,\text{mm}^2$, $3 \times 3\,\text{mm}^2$ and $4\pi\,\text{mm}^2$ cross-section. Its expected T_2 obtained with Equation 2.65 will be in concordance with the T_2 of the previous cells used in the single-photon experiment ($T_2 = 2\,\text{ms}$ [5]).

Part II

Beam shaping

Beam shapers: Gaussian to Square Top Hat

This chapter will introduce the theoretical background of the beam shapers.

In section 5.1, Gaussian beams will be introduced, followed by a brief explanation of Top Hat profiles in section 5.2. Finally, in section 5.3, several ways to transform a Gaussian beam into a Top-Hat will be explained. Precisely, *Diffractive Optical Elements.*

5.1 Gaussian Beams

The propagation of electromagnetic waves can be described by the solutions of the spatial Helmholtz equation [31] which is given by

$$\Delta A + k^2 A = 0 \tag{5.1}$$

Where Δ is the Laplacian operator, A is the amplitude, and k is the wavenumber. The eigenfunction solution of the Helmholtz equation can be written in the form of a Gaussian beam (in Cartesian coordinates) as [31]

$$A = a \frac{w_0}{w(z)} exp \left[-\frac{x^2 + y^2}{\left(\frac{w(z)}{2}\right)^2} - ikz - ik\frac{x^2 + y^2}{2R(z)} + i\zeta(z) \right] \tag{5.2}$$

Where $w(r)$ is the waist[18] of the beam, w_0 is the waist at $z = 0$, $R(z)$ describes the radius of curvature of the wavefront, and $\zeta(z)$ is the *Gouy's phase shift*[19]. Higher order eigenfunctions can be obtained as a product of a Hermite polynomial with a Gaussian function [33].

$$
\begin{aligned}
A_{lm}(x, y, z) =& a \frac{w_0}{w(z)} H_l \left(\frac{x\sqrt{2}}{\left(\frac{w(z)}{2}\right)} \right) H_m \left(\frac{y\sqrt{2}}{\left(\frac{w(z)}{2}\right)} \right) \\
& \times \exp \left[-\frac{x^2 + y^2}{\left(\frac{w(z)}{2}\right)^2} - ik\frac{x^2 + y^2}{2R(z)} + i\left(1 + l + m\right)\zeta(z) \right]
\end{aligned}
\tag{5.3}
$$

---

18. In this section of the thesis, we will use the terms waist' and 'width' indistinctly to refer to the diameter of the beam.
19. Gouy's phase shift is a phase shift that a converging light wave undergoes when passing through its focus [32]

Where H_l and H_m are the Hermite polynomials of orders l and m respectively. These eigenfunctions are denoted as lm transverse modes or TEM$_{lm}$ [34].

(a) Gaussian beam with the common definitions of waist and its intensities
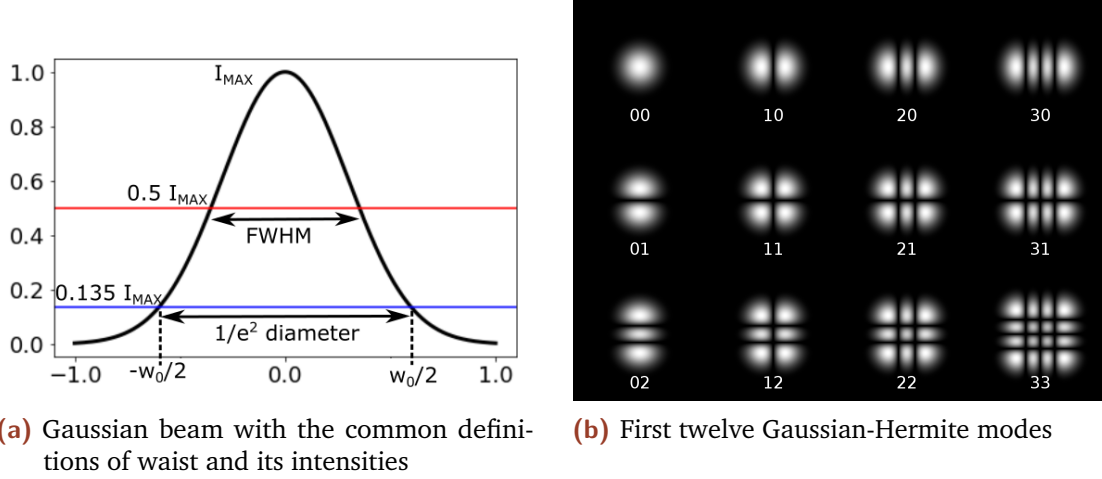
(b) First twelve Gaussian-Hermite modes

Figure 5.1.: Representation of the fundamental mode of the Gaussian beam and the twelve Gaussian-Hermite (TEM$_{lm}$) modes.
Picture extracted from [35].

The lowest mode, or TEM$_{00}$, also called fundamental mode and its amplitude is given by Equation 5.2. The imaginary part in the exponential of Equation 5.2 is related to the phase of the beam, whereas the real part is related to the irradiance of the beam [36]. The time-averaged intensity of the mode can be obtained as the square of the amplitude over two times the impedance of the propagating medium η [37]. In the case of the fundamental mode,

$$I_{TEM_{00}} = \frac{|A_{00}|^2}{2\eta} = I_0 \left(\frac{w_0}{w(z)} \right)^2 \exp \left(\frac{-2 \left(x^2 + y^2 \right)}{\left(\frac{w(z)}{2} \right)^2} \right) \tag{5.4}$$

Where I_0 is the maximum intensity of the mode.

5.1.1 Characteristics of a Gaussian beam

Width

There are several ways to define the width of a beam, and in some cases, it is useful to express the waist in terms of the FWHM [38], but commonly it is expressed as the so-called $1/e^2$ width. In this formalism, it is more intuitive to express the intensity in

cylindrical coordinates where the waist expands along with a radius r, and the beam propagates along the z-axis. Therefore in $z = 0$,

$$I(r, z = 0) = I_0 \exp\left(\frac{-2r^2}{\left(\frac{w_0}{2}\right)^2}\right) \qquad (5.5)$$

Now imposing that the radius of the beam to be half of the waist for $z = 0$, $r = w_0/2$,

$$I\left(r = \frac{w_0}{2}, z = 0\right) = \frac{I_0}{e^2} \qquad (5.6)$$

So the waist is defined as the diameter where the intensity has $1/e^2$ (13.5%) of the value of the peak intensity. A perfect collimated beam is not realistic since diffraction causes the beam to spread transversely as it propagates [34]. The following equation describes how the waist of the beam evolves along the propagation axis [36]

$$w(x) = w_0 \sqrt{1 + \left(\frac{z\lambda}{\pi w_0^2}\right)^2} \qquad (5.7)$$

Where λ is the wavelengths of the beam in the propagating media.
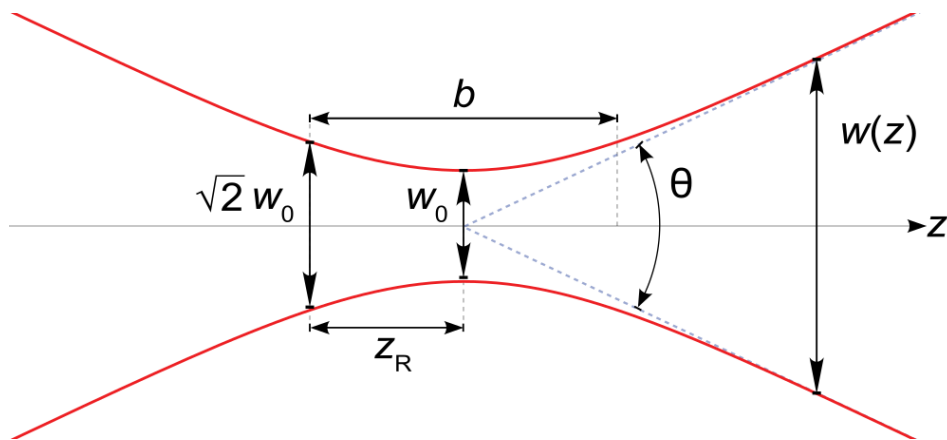

Figure 5.2.: Representation of the characteristics of a Gaussian beam. where $w(z)$ is the waist of the beam at a distance z, w_0 is the waist of the beam at $z = 0$, z_R is the Rayleigh range, b the depth of focus and θ the divergence angle.
Picture edited from [39].

Divergence angle

For large z, the Equation 5.7 asymptotically approaches

$$w(z) = \frac{\lambda z}{\pi w_0} \qquad (5.8)$$

For $z \gg \pi w_0 / \lambda$ the waist resembles an angular cone [34] with

$$\theta = \frac{w(z)}{z} = \frac{\lambda}{\pi w_0} \qquad (5.9)$$

This divergence angle describes the behaviour of the beam when propagating to infinity. θ is inversely proportional to the waist, which means better collimation will be obtained for the larger waists.

Radius of curvature

The radius of curvature describes the curvature of a spherical wavefront centred at $(x, y, z) = (0, 0, 0)$ [33]. Even if the initial wavefront was flat, during its propagation, it would gain curvature with the relation [36],

$$R(z) = z \left[1 + \left(\frac{\pi w_0}{\lambda z} \right)^2 \right] \qquad (5.10)$$

Where for z close to 0, $R \to \infty$ meaning the wavefront is a plane. And for $z \to \infty$, $R \to z$, normal for a spherical wavefront.

Rayleigh range

The Rayleigh range, or z_R is the distance where the waist of the beam has increased by a factor of $\sqrt{2}$ [33]. It can be defined as

$$z_R = \frac{\pi w_0}{\lambda} \qquad (5.11)$$

This distance, apart from having the maximum wavefront curvature, is considered the separation point of the near-field and mid-field divergence [34]. The distance between $z = -z_R$ and $z = z_R$ is called *depth of focus*.

5.1.2 Propagation factor - M^2

Pure Gaussian laser beams are nonexistent in the real world [34]. The output mode contains higher-order modes that do not propagate as the previous formulation for most lasers. The propagation factor M^2 was introduced utilising the fact that for all lasers, the product between the waist and the divergence angle is constant [34]. Thus, we define

$$M^2 = \frac{w_{0R} \theta_R}{w_0 \theta} \qquad (5.12)$$

Where the subindex R denotes the real beam. For pure Gaussian $M^2 = 1$. Equation 5.7 and Equation 5.10 can be rewritten as

$$w\left(x\right) = w_{0R}\sqrt{1 + \left(\frac{z\lambda M^2}{\pi w_{0R}^2}\right)^2} \tag{5.13}$$

$$R\left(z\right) = z\left[1 + \left(\frac{\pi w_{0R}}{z\lambda M^2}\right)^2\right] \tag{5.14}$$

M^2 quantifies how "Gaussian" a real beam is. It is used as a quality factor.

5.2 Top hat beams

One of the problems of the Gaussian beams is the low-intensity external parts of the profile known as 'wings'. These wings usually contain energy below the threshold of the desired application but still have enough energy to interact with the surroundings of the target area [40, 41].
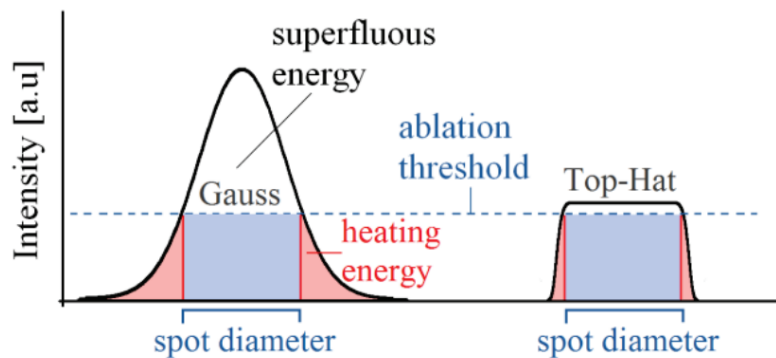
Figure 5.3.: Representation of waste power of Gaussian beams compared to a TH profile. Image obtained from [41]

For applications such as material ablation, where an intensity higher than the threshold might damage the underlying material [41], a Gaussian beam is not the most efficient profile. A profile with a homogeneous distribution of the intensity is more suitable. The steeper edges and the lack of wings reduce the surrounding interaction outside the target range [40]. Tuning the intensity of the profile to the application threshold make the so-called Top-Hat (TH) profile more efficient in these situations. Another advantage is the possibility of changing the round cross-section shape of the beam to other shapes like squares, lines, rectangles or stars during the transformation [41].

A drawback in beam-shaping a Gaussian beam into a TH is the need to add extra optical components to reshape the beam (e.g. an aperture or reflective/refractive/diffractive

elements. More details are provided in the following section 5.3). Usually, these components are highly dependent on the input beam conditions and sensitive to alignment. An exhaustive study of the effects of the misalignment is given in section 6.2. Furthermore, the TH is not invariant under transformations. The flat profile is lost as the beam propagates [40].

Often, to represent flat-top profiles, super-Gaussian are used. The equation of the super-Gaussian can be written as [42],

$$G^{(P)}(x,y) = A \exp\left(-\left(\frac{(x-x_0)^2}{2\sigma_X^2} + \frac{(y-y_0)^2}{2\sigma_Y^2}\right)^P\right) \tag{5.15}$$

for a circular super-Gaussian, and

$$G^{(P_X, P_Y)}(x,y) = A \exp\left(-\left(\frac{(x-x_0)^2}{2\sigma_X^2}\right)^{P_X} - \left(\frac{(y-y_0)^2}{2\sigma_Y^2}\right)^{P_Y}\right) \tag{5.16}$$

For a rectangular super-Gaussian. If $P_X = P_Y$, the super-Gaussian becomes squared. In Figure 5.4, it can be seen how a squared Gaussian evolves with different values of $P_X = P_Y$.
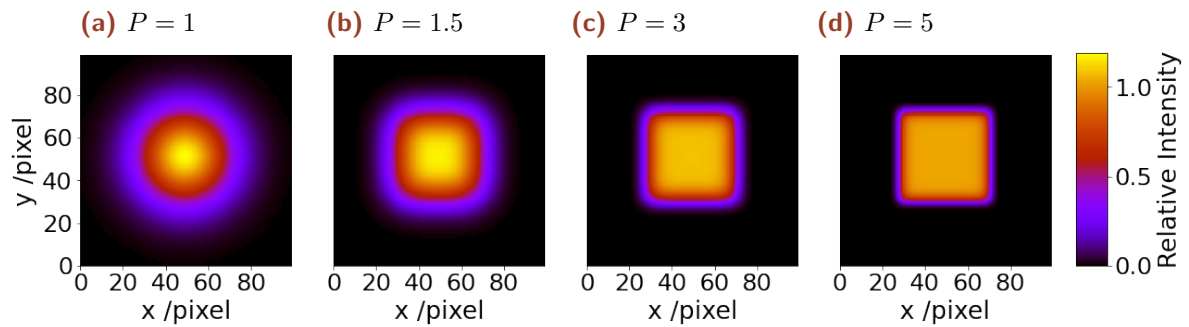

Figure 5.4.: Evolution of a super-Gaussian for different values of $P = P_X = P_Y$. For $P = 5$ the super-Gaussian resembles a squared flat profile.

As the value of P increases, the flatness of the profile increases too, and the edges become sharper.

However, for simplicity, in this thesis, we will consider the TH profile an ideal square where all the intensity is distributed homogeneously on the surface. It can be represented as

$$TH(x,y) = \begin{cases} I_{\text{TH}} & \text{if } |x-x_0| \leq a \text{ and } |y-y_0| \leq a \\ 0 & \text{Otherwise} \end{cases} \tag{5.17}$$

Where (x_0, y_0) us the centre of the TH, a is half the waist of the profile, and I_{TH} is the intensity of the profile.
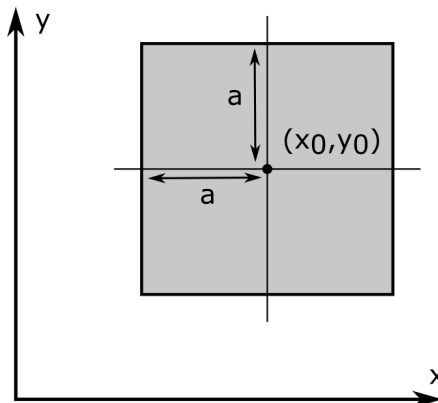

Figure 5.5.: Representation of an ideal TH of waist $w_x = w_y = 2a$, centred in the position (x_0, y_0) propagating along the z-axis.

5.3 Beam shaping a Gaussian into a Top Hat

Many techniques exist to reshape a Gaussian laser beam [43]. In this section, it will be briefly explained some of these procedures, including *Diffractive Optical Elements* (DOE), which are used in this thesis.

The most trivial way to obtain a flat beam is the use of an *aperture* [44]. The aperture is located at a flat section of the beam as shown in Figure 5.6 (a). The output size can be modified later with a telescope. The main inconvenience of this procedure is the loss of light.

A second way to obtain a TH profile is the so-called *beam integrators* [44]. Beam integrators are formed with two components

1. A sub-aperture array that splits the input beam into an array of sub-beams. It also applies a phase aberration to each sub-beam.

2. A focusing element that superposes the sub-beams in its focal plane (F in Figure 5.6 (b)).

This system is especially optimal for multimode lasers, and it can be designed to be lossless [44]. A more extensive description of these techniques can be found in [45].

A third technique of beam shaping is the so-called *field mapping*. Field mappers transform single-mode gaussian by remapping the intensity of the beam, as shown in Figure 5.7, to create a wide variety of forms [46]. This lossless transformation can be
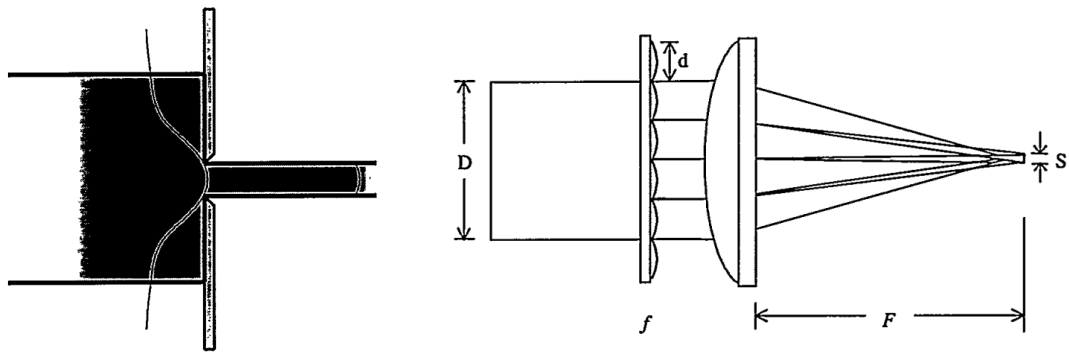
(a) Aperture applied to a beam to create a flat profile.

(b) Overlapping of the split sub-beams, after applying a phase aberration to them.

Figure 5.6.: Representation of laser beam shaping: (a) aperture technique, and (b) beam integrator.
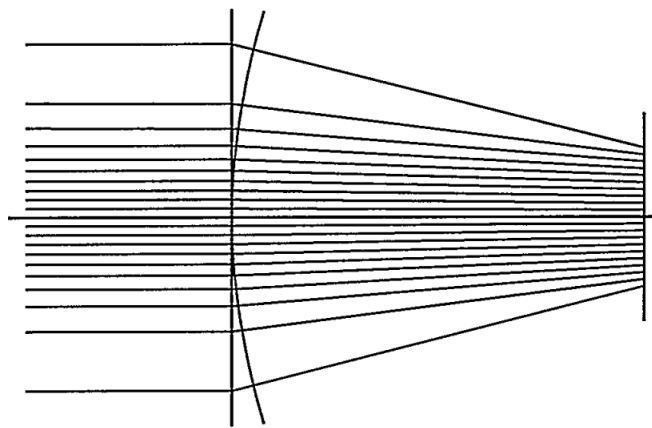Image obtained from [45]

Figure 5.7.: Representation of laser beam shaping: field mapping.
Image obtained from [45]

obtained with refractive, reflective or diffractive optics [44]. Some examples of these optics are:

- Binary diffractive optics [47]

- Two aspheric elements [48]

- Single bi-aspheric element [49]

Many other options can be found in [43].

5.3.1 Field mapping

The field mapping problem aims to determine the phase function $\psi(x_1, y_1)$ that represents the lossless beam shaping element [44]. This problem can be expressed as the in terms of the Fresnel integral as [44]

$$
\begin{aligned}
U(x_0, y_0) =& \frac{\exp(ikz)}{i\lambda z} \iint U(x_1, y_1) \exp \psi(x_1, y_1) \\
& \times \exp \left\{ \frac{ik}{2z} \left[(x_0 - x_1)^2 - (y_0 - y_1)^2 \right] \right\} dx_1 dy_1
\end{aligned}
\tag{5.18}
$$

Where where $k = 2\pi/\lambda$, λ the wavelength of the light, $U(x_1, y_1)$ represents the input beam, and $U(x_0, y_0)$ represents the shaped output beam.

In [50], Romero and Dickey provide a detailed solution for turning a circular Gaussian beam into a round and squared TH (representation of the system shown in Figure 5.9 (b)). In the solution, they expressed the phase function as $\psi = \beta\phi$, which turned the 2-dimensional problem for the squared separable into two 1-dimension solutions. Thus, $\psi = [\beta_x \phi_x(x) + \beta_y \phi_y(y)]$.

The solutions presented in [50] are, for the squared TH,

$$
\phi(\xi) = \frac{\sqrt{\pi}}{2} \cdot \xi \cdot \text{erf}(\xi) + \frac{1}{2} \cdot \exp\left(-\xi^2\right) - \frac{1}{2}
\tag{5.19}
$$

where

$$
\xi = \frac{\sqrt{2} \cdot x}{r_0} \quad \text{or} \quad \xi = \frac{\sqrt{2} \cdot y}{r_0}
\tag{5.20}
$$

And r_0 is the $1/e^2$ radius of the input beam. For the round TH,

$$
\phi(\xi) = \frac{\sqrt{\pi}}{2} \cdot \int_0^\xi \sqrt{1 - \exp\left(-\rho^2\right)} d\rho
\tag{5.21}
$$

where

$$
\xi = \frac{\sqrt{2} \cdot r}{r_0}
\tag{5.22}
$$

and r is the distance from the centre of the beam. And finally,

$$
\beta = \frac{2\sqrt{2\pi} r_0 y_0}{F\lambda}
\tag{5.23}
$$

where y_0 is half the waist of the desired profile (both circular and squared), and F is the focal length of the focusing lens.
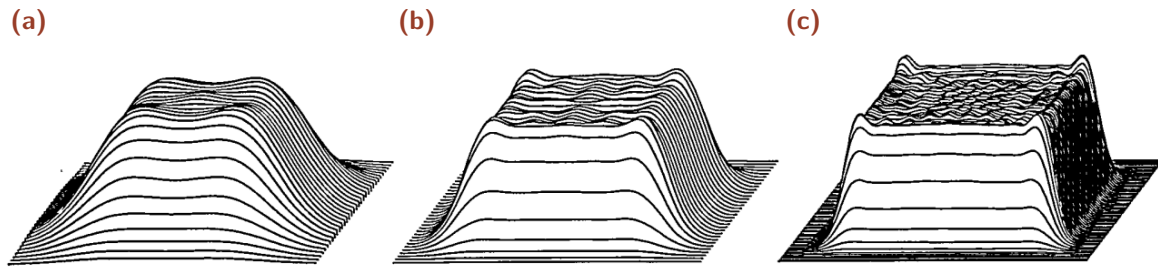
Figure 5.8.: Different squared TH field mapping solutions simulated for different β. (a) $\beta = 4$, (b) $\beta = 8$, and (c) $\beta = 16$.
Image obtained from [44]

For large β better solution of the field mapping can be obtained [44]. This can happen by increasing the input or output desired beam waist.

5.3.2 Diffractive Optical Elements

Diffractive Optical Elements use diffraction to change the distribution of light. The elements are subjected to etching processes that create specific micro- or nanostructures that cause the diffraction [40]. The effect of these structures depends on the incidence features of the beam, so each beam shaper is designed to operate under specific conditions (e.g. wavelength, input and output beam size, working distance) [40, 51]. DOEs can transform fundamental Gaussian modes (TEM$_{00}$) to any custom shape with sharp edges, but they require $M^2 < 1.3$ [51, 52].
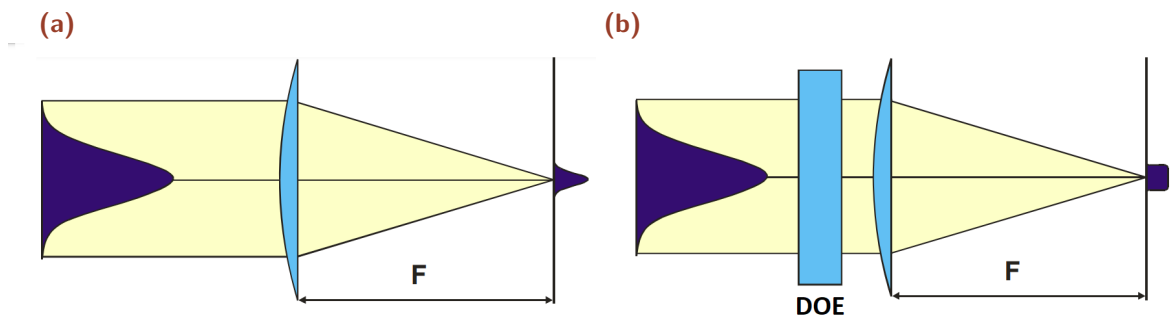

Figure 5.9.: Transformation of a focused Gaussian beam (a) to a Top Hat (b) beam by introducing a Diffractive Optical Element (DOE).
Image obtained from [43].

There are two types of DOE [52]

- *Focal beam shapers*: Hybrid of diffractive element and lens. The TH appears at the *effective focal length* (EFL) of the hybrid.

- *Angular bam shaper*: the diffractive element produces the TH at the infinity, so it is focused in a plane with a focusing system. The TH appear at the focal length of the focusing system.

Implementation of a Squared Top Hat Beam Shaper

<div style="text-align: right">**6**</div>

This chapter will review the process of the creation of a TH profile.

First, in section 6.1, the optical elements used in the experimental process will be explained. Afterwards, the alignment of the TH and its final measurement will be detailed in section 6.2 and section 6.3, respectively. Finally, the collimation of the TH will be introduced in section 6.4.

6.1 Optical elements and setup

The experimental setup used to obtain the TH is described in [52–55]. It consists of a Diffractive Optical Element (DOE) used to transform a Gaussian beam (TEM$_{00}$) to a squared homogeneous-intensity spot in a specific work plane. For angular DOEs, this work plane is determined by the focal length of the focusing system placed right after the DOE [52].

6.1.1 Beam shaper

The beam shaper used is the $GTH-4-2.2$, a DOE manufactured by TOPAG lasertechnik [54, 55]. It is an angular beam shaper, so it projects the flat-intensity profile at infinity unless we use a focusing system. The DOE has a flat angle of 2.2 mrad and requires a beam with an input diameter ($1/e^2$) of $w_{\text{in}} = 4.00 \pm 0.15$ mm. The TH will be generated at the focal plane of the focusing system placed after it. From [54, 55], we know the TH's width is determined by

$$w_{TH}^j = \frac{2.2 \cdot f}{1000} \tag{6.1}$$

where w_{TH} is the size of the TH, j is the direction of measuring, $[x, y]$ and f is the focal length of the focusing system.

6.1.2 Camera

The camera used is a $BFLY-PGE-12A2M-CS$ manufactured by FLIR [56]. The camera is powered via PoE (Power over Ethernet). This feature allows us to supply current to the camera and receive data through the same cable. The camera's size is

ultra-compact, $29 \times 29 \times 30\,\text{mm}^3$. It is monochromatic and has a resolution of 1.2 MP with pixels distributed as 1288×960. Its pixel size is,
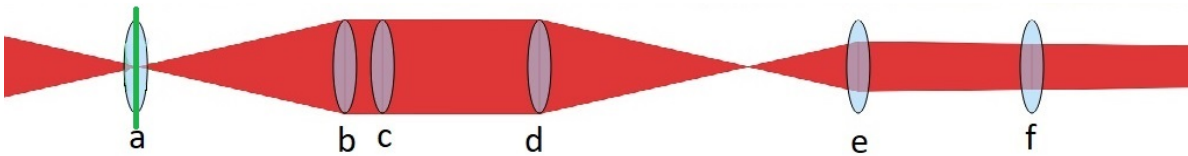
$$l_p = 3.75 \times 3.75\ \mu\text{m}^2 \tag{6.2}$$

The images obtained are stored as a Bitmap of the saturation of the pixels (from 0 to 255) due to the beam's intensity. The analysis of the pictures is performed using python.

6.1.3 Setup
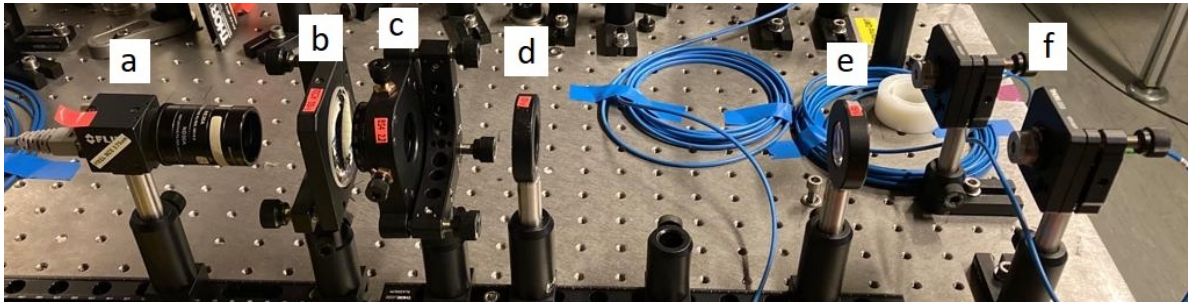
(a) Beam shaper setup.

(b) Beam shaper ray diagram.
This figure was created using J. Lodewyck's *Gaussian Beam program*.

Figure 6.1.: Optical elements of the beam shaper experiment: a - Camera, b - Focusing system lens, c - Beam shaper DOE, d,e - Resizing telescope (focal lengths of 50 and 100 mm to double the size), f - Fibre coupler. The green line in (b) is the location where the TH profile is obtained.

As shown in Figure 6.1, the experimental setup to obtain a squared TH beam consists of a DOE and a focusing system.

First, we have to produce a beam matching the specification of the DOE, i.e. a collimated beam of waist $w_{\text{in}} = 4.00 \pm 0.15\,\text{mm}$. In our case, the output beam of the fibre coupler was around half the desired waist and diverging with $\theta = 3.67$ mrad. Therefore, we used a basic telescope of magnification $m = 2$ to increase the beam's diameter to 4 mm and correct the divergence (this will be explained in more detail in section 6.2.1). The specifications of the setup are summed up at Table 6.1

Table 6.1.: Distances between the optical elements of the TH setup. The absolute distances are measured from the fibre coupler and the relative from the previous optical element mentioned.

Optical element	Absolute position /mm	Relative position /mm
Fibre coupler	0	0
$f_1 = 50$mm	83	83
$f_2 = 100$mm	244	161
Beam shaper DOE	319	75
Focusing system $f = 100$mm	337	18
Camera (TH)	437	100

Afterwards, the DOE and the focusing system are placed. We used a two-inch achromatic cemented doublet[20] of $f = 100$ mm. Finally, a camera records the profile. It will be formed at the focal plane of the focusing system, which is equal to its focal length. In this case, at 100 mm after the lens. According to Equation 6.1, the size of the TH would be,

$$w_{\text{TH}} = 220 \times 220\,\mu\text{m}^2 \tag{6.3}$$

This is equivalent to 59×59 pixels.

6.2 Alignment

NOTE: Some of the figures in this section are inspired or taken from [52].

The more crucial part of obtaining a TH profile is the alignment of the lenses. But first, we must ensure the input beam matches the specifications.

6.2.1 Input beam

As stated in section 6.1.3 the output beam of the fibre coupler was $w_{\text{out}} = 1.82$ mm with a divergence angle of $\theta = 3.67$ mrad. Thus, we needed to compensate for the divergence and double the size of the beam.

As shown in Figure 6.2a, if the input beam is collimated, its size can be doubled with a simple two-lens telescope of augmentation $m = \dfrac{f_2}{f_1} = 2$. This is obtained with two

---

20. An achromatic cemented doublet consists of two lenses cemented together. Usually, one is convex and the other concave. These lenses are computer designed to minimise spherical aberration and coma effectively. As a result, doublet lenses have superior optical performance than singlet lenses. They offer better broadband and off-axis performance and nearly constant focal length across the spectrum [400,1100] nm. In an achromatic doublet, the chromatic aberration is compensated using glasses of two different refractive indexes [57].

lenses, one with focal length f and the second with $2f$. The separation of the lenses must be equal to the sum of both lenses' focal lengths. E.g. one of focal length $f_1 = 50$ mm and another of $f_2 = 100$ mm separated a distance $d = 150$. Indeed, in this case, $m = \dfrac{100}{50} = 2$.
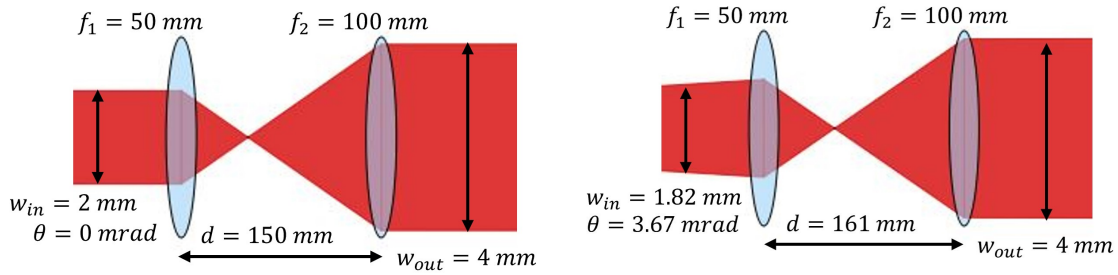
(a) Resizing a collimated 2 mm beam to 4 mm with a telescope of $m = 2$.

(b) Resizing a beam of 1.82 with a divergence of $\theta = 3.67$ mrad to a collimated 4 mm beam.

Figure 6.2.: Comparison between: (a) resize a collimated beam, (b) resize and off-collimated beam.

The beam divergence could have been compensated with the adjustable lens of the fibre coupler. However, the collimated size was $w_{\text{out}} = 1915\,\mu$m. To reach the $4\,$mm, we needed a telescope of augmentation $m = 2.09$, and it would require lenses with precise focal lengths. Instead, we took advantage of the divergence and compensated for these defects by increasing the distance between the two lenses. The final separation between the lenses was $d = 161$ mm (see Figure 6.2b). Once the beam matches the specifications, we are ready to place the rest of the elements as described in section 6.1.3.

6.2.2 Alignment

Following the steps of [52], the easiest way to proceed was to fix the focusing system and locate its focal plane before placing the DOE. Afterwards, put the DOE, align it to the beam and the focusing system, and record the TH with a camera.

The focal plane of the focusing system can be found using a camera or a waistmeter. The focal plane is where the beam size is reduced to the minimum. Theoretically, it is placed at a distance equal to the lens' focal length.

Once the focal plane is located, we placed the beam shaper right before the focusing lens. A TH profile would appear at the found focal plane if the focusing system, the DOE and the beam are perfectly aligned. Unfortunately, this is unlikely to happen.

Mounting the DOE in a 6-axis kinematic mount allowed us to correct the misalignment. The mount enables adjustments in displacement and rotation along the three-axis: x, y, and z.

During this section of the thesis, the convention of axes we will use is z, the direction of propagation of the beam and x and y, the horizontal and vertical directions perpendicular to the z-axis, respectively.

The leading causes of the misalignment are:

- Misplacement of the DOE towards the beam in the x/y plane (Adjustment: x/y position and tilt)

- Recording the TH with the camera before/after the focal plane of the focusing system, i.e. the position where the TH is created (Adjustment: z position)

- Input beam smaller/bigger than the specified (Adjustment: beam size)

6.2.2.1 x/y position and tilt

If we have a tip/tilt or an x/y misalignment of the DOE, the intensity allocates uneven on the square profile, as shown in Figure 6.3. In this case, the TH's shape and size remain the same.
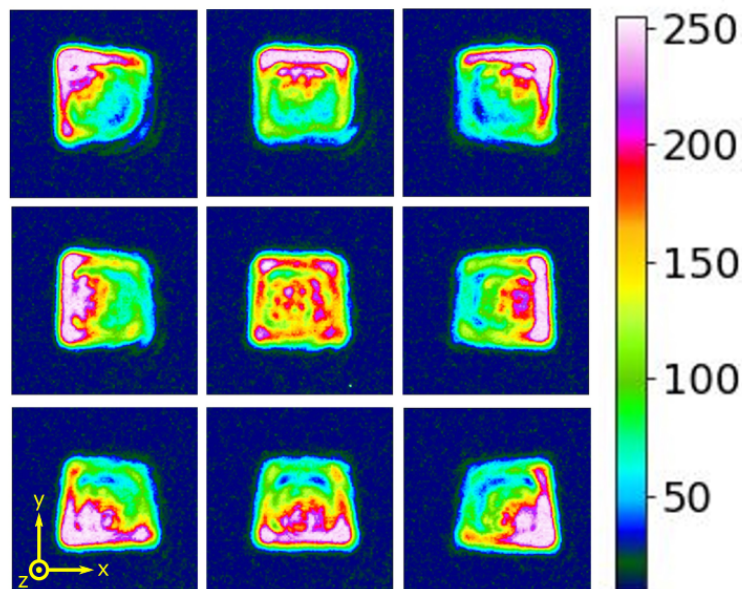

Figure 6.3.: Misalignment on x/y axis / tilt-tip of the DOE. The size of the TH is roughly 203 x 206 μm. The colour bar goes from 0 to 255 of the saturation of each pixel. This is useful for qualitatively showing how the light is distributed along the entire profile.
This picture is inspired by the one in [52].

The profile in the central picture of Figure 6.3 is not entirely flat. The size determined for this TH was $w_{\mathrm{TH}} = 203(3) \times 206(3)\ \mu\mathrm{m}^2$. It was slightly smaller than expected. These indicated the beam was not aligned yet. It needs further adjustments. However, the shape of the beam was now squared. And the intensity was distributed across the whole profile. In section 6.3, we will introduce how to estimate the quality of the obtained TH profile.

6.2.2.2 z position

As mentioned before, the TH is only created at the focal plane of the focusing system. Hence, the TH profile can not be observed outside the focal plane. Shown in Figure 6.4 and Table 6.2, there are the representation and the characteristics of this misalignment.
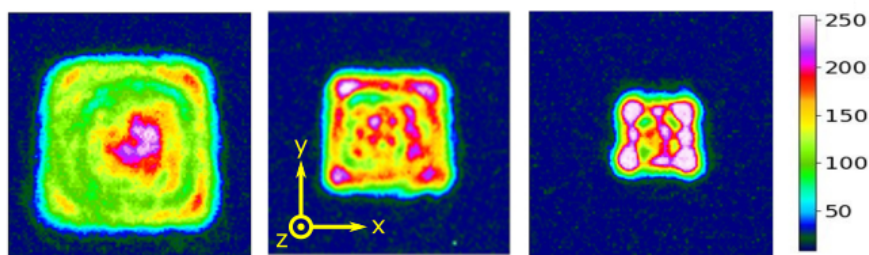

Figure 6.4.: Misalignment on z- axis (Before the TH position, at TH and after TH). The pictures are on scale for a better comparison. Sizes are written in Table 6.2.
This picture is inspired by the one in [52].

Table 6.2.: Characteristics of the misalignment on the z-axis. The column 'Distance' refers to the distance between the DOE and the obtained image.

Position	Distance /mm	Size /μm	Profile
Before TH	85	$261 \times 272\ (\pm 3)$	Convex
At TH	100	$203 \times 206\ (\pm 3)$	TH
After TH	115	$153 \times 125\ (\pm 6)$	*Dog-ears*[21]

As we see, before the proper position, the TH is bigger and convex and after is smaller and has dog-ears.

6.2.2.3 Beam waist

A deviation from the required input beam waist (4 mm in our case) can lead to a deformation of the TH too. When the beam is smaller, the profile becomes larger and

---

21. [table] Dog-ears refer to a profile where the mid-part has a lower intensity than the corners or edges.

more convex, and when the beam is bigger, it becomes smaller and with dog-ears, as we see in Figure 6.5 and Table 6.3.
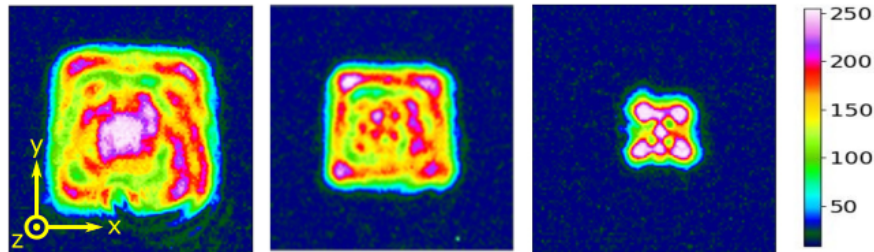

Figure 6.5.: Change in the input beam size (smaller, correct and bigger). The pictures are on scale for a better comparison. Sizes are stated in Table 6.3.
This picture is inspired by the one in [52].

Table 6.3.: Characteristics of the change of the input beam size. *Dog-ears refer to a profile where the mid-part has a lower intensity than the corners.

Beam size	Size /μm	Profile
Smaller	246×254 (± 3)	Convex
4 mm	203×206 (± 3)	TH
Bigger	116×123 (± 9)	Dog-ears

As we see comparing Figure 6.4 and Figure 6.5. Having a small input beam causes the same defects as recording the TH before its ideal position (Bigger and convex profile). Having a larger beam or recording the TH after the ideal position causes the same defects (Smaller profile and dog-ears.).

In Figure 6.6, it is more clearly seen how the beam's profile evolves while we move along its propagation axis (z-axis). Before the proper position, the profile exhibits more curvature in the edges. After this position, the intensity is more distributed to these edges than the centre creating the dog-ears.
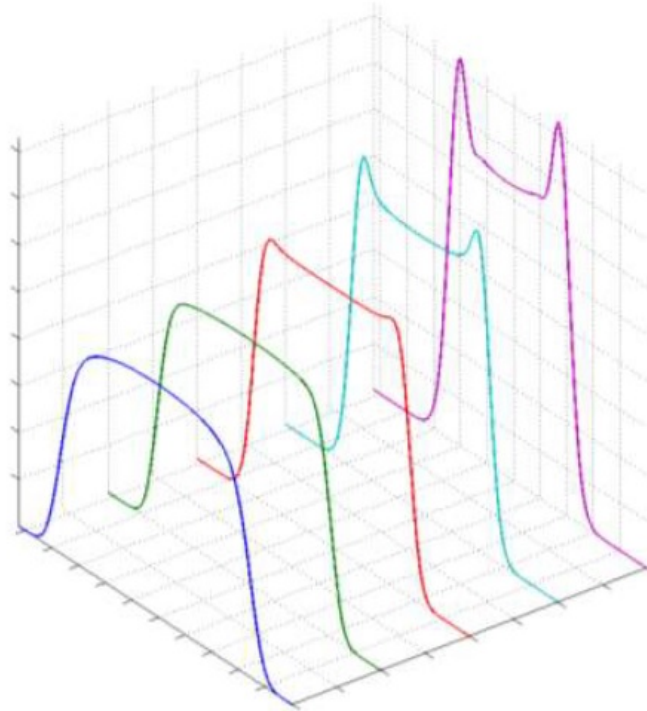
Figure 6.6.: Evolution of TH profiles along z-axis. It exhibits the curvature change from convex (dark blue and green) to TH (red) to dog-ears (light blue and purple).
This picture is extracted from [52].

6.3 Analysis and final TH

To determine the best approximation to a squared flat profile, we compared the standard deviation of the obtained profile subtracted from an *ideal* TH. But first, we had to determine what this ideal TH is. Therefore, we determined what size and intensity our profile had.

6.3.1 Intensity and size

From [54, 55], we know that 95% of the input power applied to the beam shaper is distributed along the TH. Thus, we can consider the other 5% distributed on the wings of the TH. To find the threshold value separating the wings from TH, we integrated the pixels from lowest to highest values until we reached 5% of the total power (integral of the whole picture). Then, we determined the intensity by averaging the values above the threshold. Additionally, we computed an acceptance range by calculating the standard deviation (STD). We computed the background the same way but with the values below the threshold.

The intensity is normalised to the maximum saturation level of the camera's pixels. Hence, all intensities from now on will be given in units of relative intensity (r.i.). Then, the computed amplitude (intensity) of the ideal TH is,

$$A_{\mathrm{TH}} = 0.468 \pm 0.002 \text{ r.i.} \tag{6.4}$$

The error on the amplitude can be estimated from the STD divided by the squared root of the number of samples.

$$\delta X = \frac{\sigma_X}{\sqrt{N}} \tag{6.5}$$

Where δ_X is the uncertainty of a given variable X, σ_X is the STD of X, and N is the number of samples.

In the following, we present an exemplary approach to determine which pixels numbers the TH profile starts and ends to determine its size for the x-direction. For y-direction was done the same way but on the vertical axis. y results are stated after x approach and results.

(a) TH with 5% x and y external ranges marked.
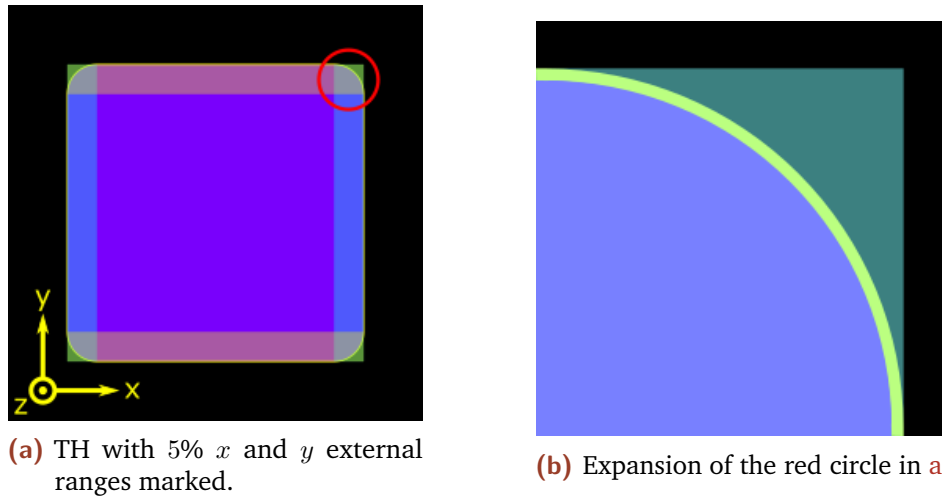
(b) Expansion of the red circle in a

Figure 6.7.: TH with round corners and x (blue) and y external (pink) range coloured. The ranges correspond to the initial and final 5% of the profile.

We started determining in each row at what pixel number the intensity changes from background and wings to TH (p_i) and from TH to background and wings again (p_f). We neglected the rows with only background. As the edges were not entirely straight and the corners were round (see Figure 6.7b), we discarded the first and the last 5% rows (pink areas in Figure 6.7a). In those pink areas, the curvature of the corner modified the pixel number where the intensity increased/decreased. As we computed the p_i and p_f of the ideal TH as the average of the p_i and p_f measured in every row, the pixels in

those curves would falsify the value. Thus, the mean and the STD were computed only in the inner horizontal 90% range (blue and purple areas of Figure 6.7a). In the y case, we discarded the background and the first and last 5% of the columns (blue areas in Figure 6.7a) and did the mean and STD from the inner vertical 90% (pink and purple areas in Figure 6.7a).

$$
\begin{aligned}
p_i^X &= 17.00 \pm 0.07 \text{ pixels} \\
p_f^X &= 78.47 \pm 0.09 \text{ pixels}
\end{aligned}
\tag{6.6}
$$

Finally, we computed the size by subtracting both pixel positions and multiplying by the pixel size as in Equation 6.7.

$$
w_{\mathrm{TH}}^j = \left(p_f^j - p_i^j \right) \cdot l_p^j
\tag{6.7}
$$

Where w_{TH} is the TH width, p_i is the pixel where the intensity increases from background to TH, p_f is the pixel where the intensity decrease to the background again, l_p is the pixel size (Equation 6.2) and j is the direction in which we measure, $[x, y]$. Its uncertainty can be computed with the error propagation formula,

$$
\delta_{f(x1,x2,\dots)} = \sqrt{\sum_{i=1}^{n} \left(\frac{\partial f}{\partial x_i} \right)^2 \delta_{x_i}^2}
\tag{6.8}
$$

as

$$
\delta_{w_{\mathrm{TH}}} = \sqrt{\left(\delta_{p_f}^2 + \delta_{p_i}^2 \right) l_p^2 + (p_f - p_i)^2 \delta_{l_p}^2}
\tag{6.9}
$$

Where we supposed the pixel error to be 1% of the pixel size and the error of the increasing and decreasing pixels are taken from Equation 6.6. The representation of these ideal THs in the x-direction and some random TH 'slices' from our measure are shown in Figure 6.8a.
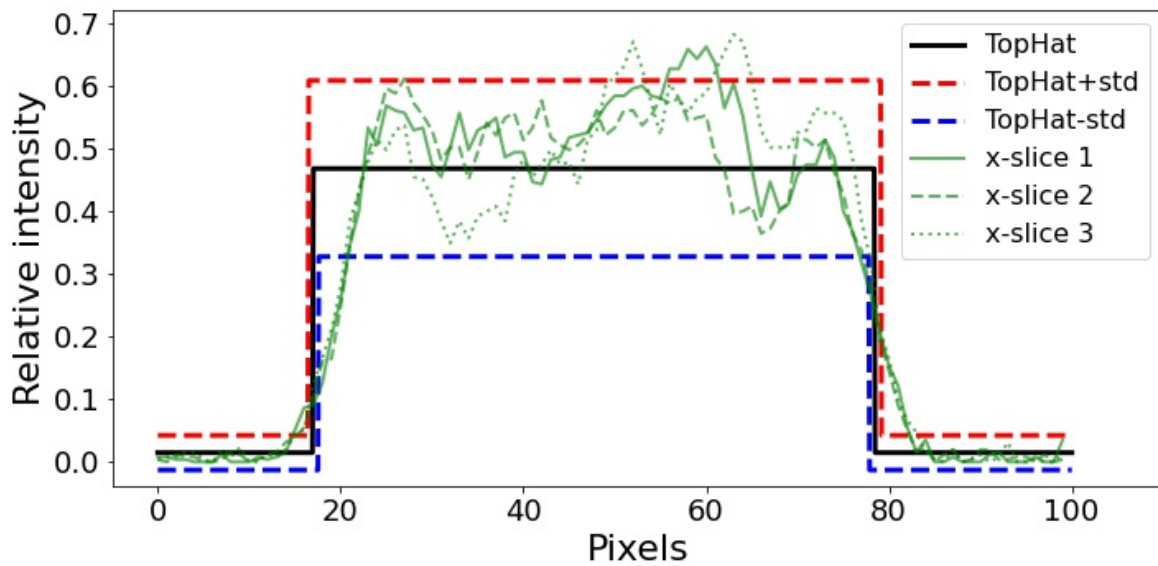
The same procedure was done to obtain the width in the y (vertical direction) with the pixels,

$$
\begin{aligned}
p_i^Y &= 18.14 \pm 0.09 \text{ pixels} \\
p_f^Y &= 79.70 \pm 0.09 \text{ pixels}
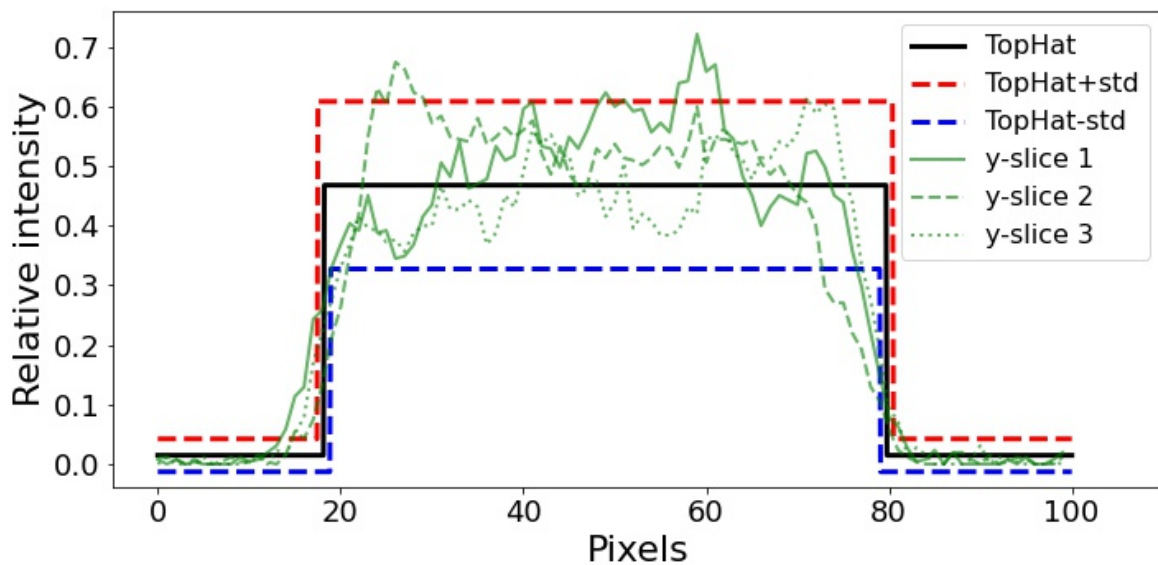\end{aligned}
\tag{6.10}
$$

Hence, the size of out TH was,

$$
\begin{aligned}
w_{\mathrm{TH}}^X &= 231 \pm 2 \ \mu\text{m} \\
w_{\mathrm{TH}}^Y &= 231 \pm 2 \ \mu\text{m}
\end{aligned}
\tag{6.11}
$$

The representation of these ideal THs in the y-direction and some random TH 'slices' from our measure are shown in Figure 6.8b.

(a) x profiles.

(b) y profiles.

Figure 6.8.: Representation of the ideal x (a) and y (b) TH profile with three random slices of the th measured. The black line represents the ideal TH calculated. The red and blue lines represent the acceptance ranges of the ideal TH calculated adding (red) and subtracting (blue) the respective STD.

To see if our profiles resemble more a TH or a Gaussian, we can compute the STD of the difference between various profiles with the ideal TH and an ideal Gaussian. The ideal Gaussian was modelled from the power and amplitude of the ideal TH. The total

power of a slice was computed by doing the integral of the 1D function. The Gaussian integral in the equation was retrieved from [15]. In this case,

$$
\begin{cases}
W_{\text{TH}}^{(1D)} = A_{\text{TH}} \cdot w_{\text{TH}}^X \\
W_{\text{gauss}}^{(1D)} = A_{\text{gauss}} \sqrt{2\pi} \sigma_{gauss}^X
\end{cases}
\tag{6.12}
$$

Where $A_{\text{TH/gauss}}$ is the amplitude of the TH/Gaussian and σ_{gauss}^X is the STD of the Gaussian. Apart from having the same power, we wanted that they were comparable in size. Using the waistmeter we determined the waist of the Gaussian to be,

$$
w_{gauss} = 4 \cdot \sigma_{gauss}^j
\tag{6.13}
$$

with j being the direction measured, $[X, Y]$. Imposing that both waists had to be equal, we solved the amplitude of the Gaussian to be,

$$
A_{\text{gauss}} = A_{\text{TH}} \frac{4}{\sqrt{2\pi}}
\tag{6.14}
$$

In Figure 6.9 we can see the qualitative comparison of a 1D TH and Gaussian with the random slices in the x-direction. In Table 6.4 we can compare the STD of difference between each slice and the ideal contours.
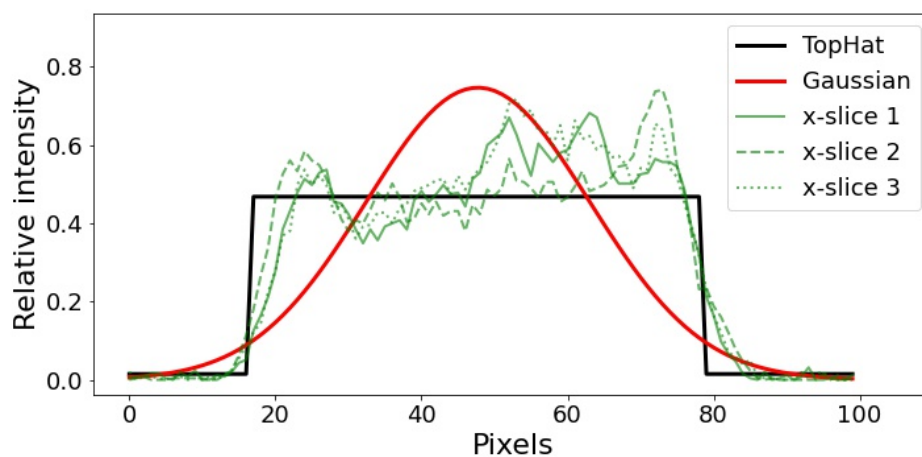

Figure 6.9.: Comparison between the ideal TH (black) and Gaussian (red) with the random slices (green) in the x-direction. The STD of the difference can be found in Table 6.4.

Table 6.4.: Standard deviation of the difference of the TH and the Gaussian contour with three random slices in the x-direction. Note that the STD with that TH is at least 1.5 times smaller in all the cases.

Shape	STD slice 1 /r.i.	STD slice 2 /r.i.	STD slice 3 /r.i.
Gaussian	0.160	0.199	0.154
TH	0.095	0.086	0.103

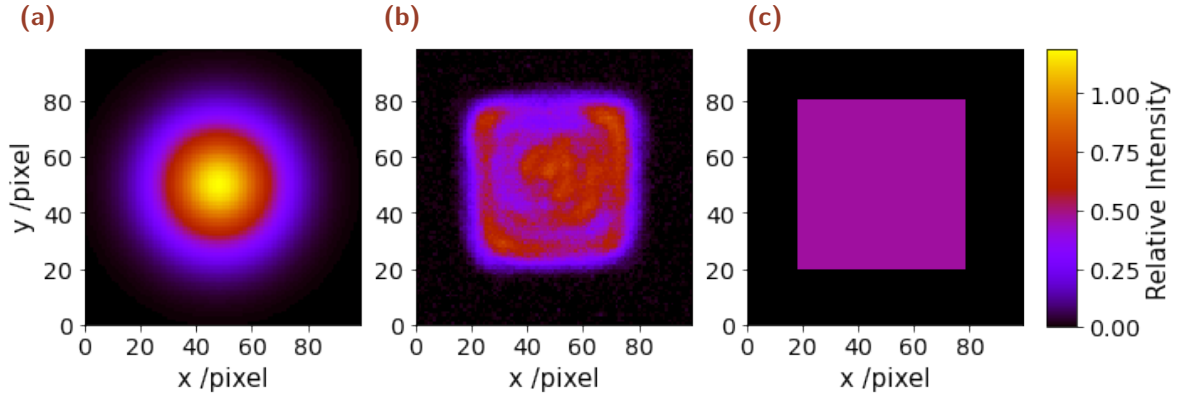In the following, we wanted to extend our description to the whole TH profile, extending from 1D to the 2D case.

(a)   **(b)**   **(c)**

Figure 6.10.: Comparison between: (a) the ideal Gaussian, (b) our profile and (c) the ideal TH in 2D.

Similar to 1D, we compared the total power of a 2D TH with the equivalent 2D Gaussian in size by integrating the 2D profile. The Gaussian integral in the equation was retrieved from [15]. In this case, the powers were,

$$\begin{cases} W_{\text{TH}}^{(2D)} = A_{\text{TH}} \cdot w_{\text{TH}}^{X} \cdot w_{\text{TH}}^{Y} \\ W_{\text{gauss}}^{(2D)} = A_{\text{gauss}} 2\pi \sigma_x^g \sigma_y^g \end{cases} \tag{6.15}$$

Imposing that the x and y waist of both beams had to be the same and using Equation 6.13, we found,

$$W_{\text{TH}}^{(2D)} = A_{\text{TH}} \cdot \left(4 \cdot \sigma_x^g\right)\left(4 \cdot \sigma_y^g\right) = 16 \cdot A_{\text{TH}} \cdot \sigma_x^g \cdot \sigma_y^g \tag{6.16}$$

Equalising Equation 6.15 and Equation 6.16, we find the relation between the amplitudes in the 2D representation.

$$A_{\text{TH}} = \frac{8}{\pi} \cdot A_{\text{gauss}} \tag{6.17}$$

With this relation, we plotted and compared the 2D ideal profiles with the one obtained in the experiment. The 2D representation can be found in Figure 6.10, and the STD comparison in Table 6.5. For a better comprehension of the shape of the beams, a 3D plot has been added in Figure 6.11, where the redistribution of energy can be better (qualitatively) appreciated.
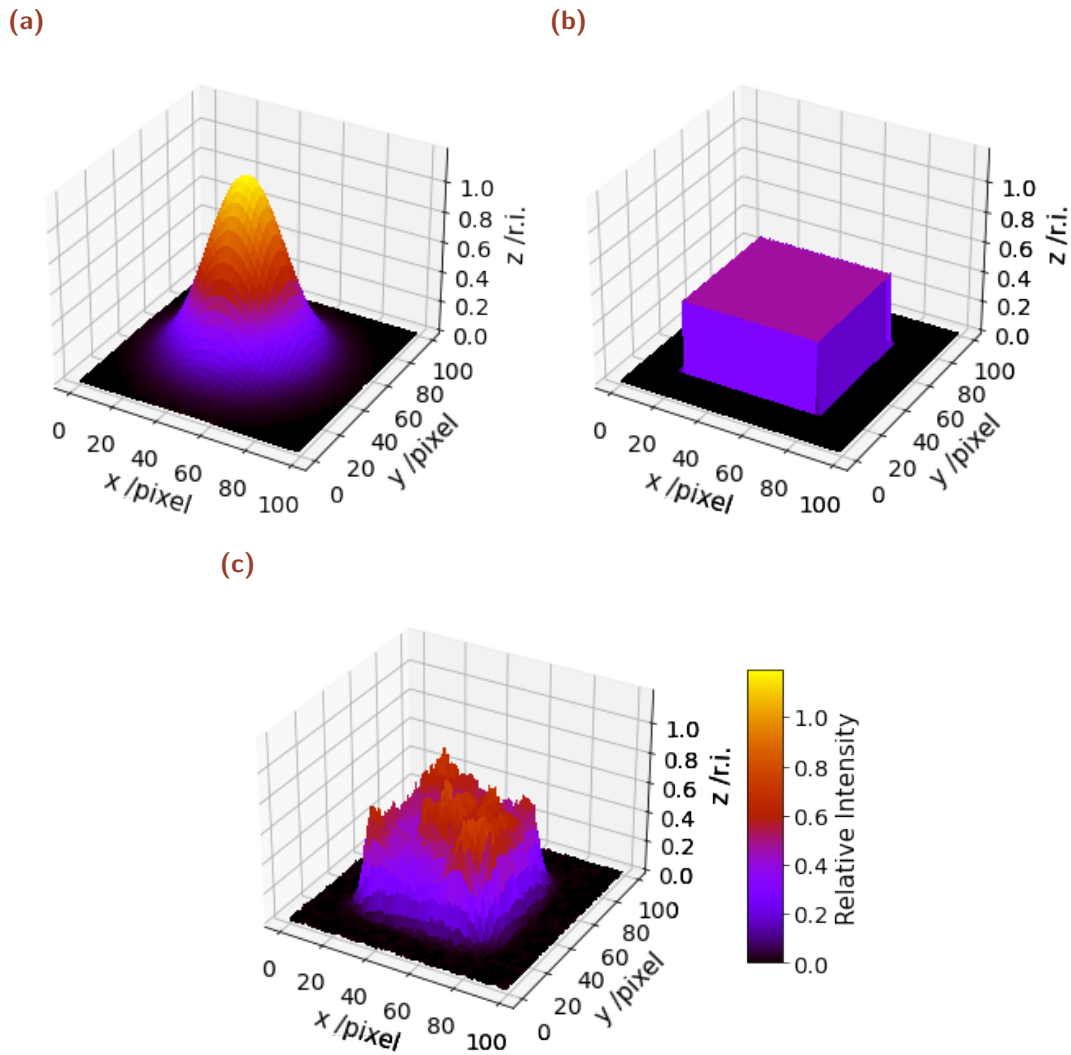

Figure 6.11.: Comparison between: (a) the ideal Gaussian, (b) the ideal TH and (c) our profile in 3D.

Table 6.5.: Standard deviation of the difference of the TH and the Gaussian contour with the obtained profile. Note that the STD with that TH is smaller.

Shape	STD /r.i.
Gaussian	0.167
TH	0.096

Note that the STD when subtracting the ideal TH to our profile is **1.74** times smaller than with the ideal Gaussian. This verifies that the beam is closer to a TH profile than a Gaussian.

6.4 Collimation

With the DOE and the experimental setup described before, we obtained a TH profile in the focal plane of the focusing system. However, in our experiments, we might be dealing with cells with an 80 mm long channel. Thus, we need a way to collimate the TH.

To collimate the TH into a squared beam of a desired waist, we needed four lenses. The first lens compensated the divergence angle of the DOE and focused the TH (we referred before to that lens as the focusing system), the second collimated the beam, and the third and fourth lenses formed a Keplerian telescope to resize the TH beam. We could reduce these four lenses to two (see Figure 6.12) with the help of a program designed by Christian F. Bærentsen. The program employed the *ABDC matrix* formalism (see Appendix A) to return the distances between two lenses of a given focal and the DOE to create a collimated TH of a desired waist. In concrete, it returned three distances:

1. The distance between the DOE and the first lens (focusing lens).

2. The distance between the first and second lens (collimation lens).

3. The distance from the second lens where we obtained the TH with the desired waist.

As the divergence of the DOE is $2.2\,\mathrm{mrad}$, the distance between the DOE and the focusing lens is not very relevant. On the other hand, we experienced the distance between the focusing lens and the collimation lens to be extremely sensitive. The third distance is the point where the desired TH will be created (EFL). As mentioned before in the theory part, the perfect collimation does not exist, and the TH is not an exemption. The 'collimated' beam obtained was still diverging, and hence the waist was not maintained along z.

6.4.1 Experimental setup

To test the collimation, we aimed for a collimated beam of $w = 1.3$ mm created using two lenses of focal lengths $f_1 = 100$ mm (focusing lens) and $f_2 = 45$ mm (collimation lens). The program returned the distances shown in Table 6.6.

Table 6.6.: Distances between the DOE and the lenses ($f_1 = 100$mm and $f_2 = 45$ mm) to obtain a collimated TH of $w = 1.3$ mm.

Distance measured	Distances /mm
DOE to f_1	186.9
f_1 to f_2	152.6
f_2 to TH	310.9

To record the profile of the collimation, we switched from the FLIR camera to a Thorlabs beam profiler[22]. The FLIR camera presented some interference patterns caused by the attenuators placed in front of the camera, making the beams' analysis impossible. However, the interference did not affect the non-collimated TH because its size was an order of magnitude lower. Another benefit is that for the working wavelengths, the beam profiler power range extends from tens of μW to 1 W [27]. Therefore, we are not power limited as with the FLIR camera. Unfortunately, this has a drawback. The images obtained with the beam profiler are recorded as bitmaps that store the intensity from 0 to 255. Thus, the intensity resolution will decrease as the power applied increases. The usage of the beam profiler was introduced in the collimation part because it was not available before. For more rigorousness, we would have already used the beam profiler for the TH alignment if we had it.
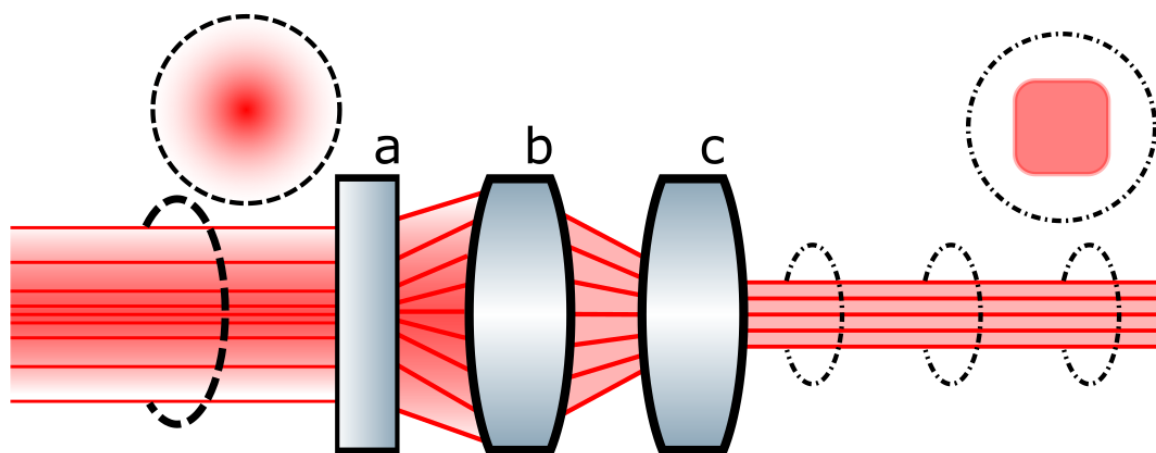

Figure 6.12.: Experimental setup to convert a Gaussian beam into a collimated Top Hat. In the image: a - Beam shaper (DOE), b - Focusing lens, and c - collimation lens.

6.4.1.1 Collimation results

In the process of the collimation, we found two interesting results. For a distance between the focusing and the collimation lenses (f_1 to f_2 in Table 6.6) of D = 153

---

22. THORLABS BP209-VIS/M [27]

mm we find that the TH profile was maintained for 180 mm. However, the waist of the beam was bigger ($w_{col} \sim 2100\,\mu$m) than what we expected from the program ($w \sim 1.3$ mm). Moreover, the collimation of the TH was produced further than the EFL predicted by the program (distance f_2 to TH in Table 6.6, EFL ~ 310.6 mm) too. For this case, the beam diverged $\theta = 0.24$ mrad.

The other interesting result happened for D = 156 mm. With this configuration, the waist of the TH at the EFL matched the description of the program. However, the TH was only maintained for around 80 mm, and its waist decreased noticeably. The divergence angle computed for this configuration was $\theta = 2$ mrad. So we could see that the beam was not collimated.

The results of both configurations are resumed in the following Table 6.7.

Table 6.7.: Results of the two possible configurations for the collimation. In the table the two configurations are represented. For each configuration, we state the distance D between the focusing and the collimation lens, the position where the collimated TH begins until it ends relative to the collimation lens and the length of this collimation, the waist during this collimation, and the divergence angle.

Distance D /mm	Collimation /mm			Waist /μm			Diver. /mrad
f_1 to f_2	Initial	Final	Length	Initial	Final	Δ Waist	θ
153	410	590	180	2076	2115	~ 40	0.24
156	280	360	80	1375	1190	~ 160	2

In Appendix B, there is a compilation of the images obtained for these two configurations[23],

6.5   Discussion

In this part of the thesis, we covered the creation of a Top Hat profile from a Gaussian beam with a DOE, and explored a way to collimate it. In this section, we shall discuss the results found and their implications.

Top Hat

For the TH, we focused on the experimental setup and creation of the profile and the analysis of its resemblance to a squared homogeneous profile.

In principle, the experimental setup seemed relatively simple. We could effectively obtain a TH with only two lenses: a DOE and a focusing system. However, getting a

23. Images gathered by Rebecca Schmieg.

beam that matched the specifications of the DOE and the alignment of the lenses was demanding. Imperfections in the collimation and the size of the input beam impaired the homogeneity of the profile. Any misalignment caused a redistribution of the power leading to an increase in the inhomogeneity of the profile. Precise alignment and iterative optimisation of the placement of the optics were therefore required.

Alignment had to be taken into account when sizing the profile, too. Not having rotational symmetry made the analysis of the profile more cumbersome. The model created was prepared for a squared profile aligned with the x-y axes. The size is determined by averaging the pixel where the TH starts and ends in each row. For rotated TH (e.g. diamond), the pixel where the TH starts, and end are different since a square is not rotational symmetric. Thus, the horizontal and vertical waist obtained would not fairly represent the TH. The graphical representation and the comparison in 2D and 3D (see Figure 6.10 and Figure 6.11) are modelled from the data obtained from the profile. Therefore, its representation will not be a fair depiction either.

Regarding the quality of the TH, we have seen in Table 6.4 that the STD of three random slices inside the profile was at least 1.5 times smaller when compared with a perfect TH than with a Gaussian. In Table 6.5 we have seen that the STD of the whole profile compared with an ideal TH was 1.74 times smaller than compared to a Gaussian. That indicated that our profile resembles more a TH than a Gaussian.

To further improve the quality of the TH (i.e. enhance homogeneity), we will need to check the quality of the input beam. Not having a perfect input beam, well collimated, with the required size and without ellipticity, will lead to inhomogeneity in the intensity distribution of the squared TH. Furthermore, the more lenses the beam crosses, the more imperfections are introduced to the beam (e.g. by optical aberration).

Finally, it should be noted that from Table 6.2, it can be seen that the creation of the TH profile is very sensitive to the distance after the focusing system. We can see that in a range of 3 cm, we went from the convex profile (pre-TH) to dog-ears profile (post-TH). The TH is maintained less than 3 cm.

Collimation

For the collimation, we see that we could collimate the beam by just adding a collimation lens. However, we obtained two interesting results. With one, the collimation was better, but its waist and position did not match the program's predictions. Then, the other matched the position and waist predicted by the program, but the collimation was worse.

For future experiments, the best configuration is the first one (D= 153 mm in Table 6.7). First of all, the new cell that will be implemented in the single-photon experiment will have a length of 80 mm. We would expect, then, collimation that exceeds that length. For the second case, D = 156 mm, we see that the collimation is maintained less than 80 mm, so this would not be a suitable option. Even though we know where it will be created and its waist.

The problem of the configuration that provides the good collimation is that the profile seems to have a lower intensity distribution in the corners. The cause and solution to these fainted corners remain to study in the future development of the collimation. A first guess would be that the input beam is not exactly 4 mm or that the input beam presents some ellipticity and its horizontal and vertical waist are not exactly the same.

To overcome the problem of the unknown waist and position of the collimated TH, it will be necessary to try the setup beforehand with the same laser we are going to use but without the rest of the experiment. Then, the location and size of the TH need to be checked. Once we know the distance of the two lenses to create the TH and the position where the TH is collimated, it would be ready to be implemented in the experiment. First, the distance between the focusing and the collimation lens would be fixed, and then the lenses placed at the correct separation from the cell to ensure the TH appears in the region where the cell is. As the distance between the DOE and the focusing lens is not critical, the beam shaper could be placed in any suitable place before the collimation system.

Conclusion and outlook 7

This thesis aimed to implement a method to reshape a fundamental Gaussian beam to a squared profile with a homogeneous distribution of the intensity and collimate that profile to be used in the next iteration of the on-demand single-photon source as presented in [5].

On the new setup proposed for the single-photon experiment, the cell cavity will be removed, and replaced by a new larger cell, more precisely, one with a length of 80 mm and a cross-section of 2×2, 3×3 or 4π mm^2. With the cell characterisation, we have proved that the fabricated cells of these dimensions have an atomic density of the order of $\rho \sim 10^{16}$ m^{-3} at room temperature ($N_a \sim 10^{10} - 10^{11}$ atoms), a transmission above 95% and depopulation times of between 5 to 20 ms. Moreover, we can expect up to double this time for the decoherence time T$_2$. Which will be at least an order of magnitude higher than the microcell used in the old setup (T$_2^{old}$=2 ms [5].)

For the main part of this thesis, a Top Hat profile was implemented. In section 6.3, we successfully demonstrated the viability of obtaining a TH with a DOE and a focusing system. In section section 6.4 we collimated the TH with a magnification factor by adding an additional lens.

The result obtained in the collimation and the collimation process itself need further studying since we observed a discrepancy between the obtained and expected result (see section 6.4). Two possible configurations have been obtained to collimate the beam. However, for implementing the TH in the single-photon experiment, only the collimation with the separation between the focusing lens and the collimation lens D = 153 mm provided a collimation long enough (along ~ 180 mm). The collimation provided by the other configuration (along ~ 70 mm) was not long enough to cover the whole cell (80 mm).

The homogeneity of the intensity and the increase of the filling factor introduced with the Top Hat should speed up the motional averaging. Therefore, the next step in the investigation will be to see if, indeed, with the TH beam, the motional averaging is accelerated and the broadband contribution of the 'write' spectrum decreased. Leading to an improvement of the write efficiency, meaning the ratio between coherent write and total spectrum. For the cells with round channels, a beam shaper with a rounded flat profile shall be tried.

Bibliography

[1] K. Jensen, M. Zugenmaier, J. Arnbak, H. Stærkind, M. V. Balabas, and E. S. Polzik. 'Detection of low-conductivity objects using eddy current measurements with an optical magnetometer'. In: *Physical Review Research* 1.3 (2019), p. 033087.

[2] H. Krauter, D. Salart, C.A. Muschik, J. M. Petersen, H. Shen, T. Fernholz, and E. S. Polzik. 'Deterministic quantum teleportation between distant atomic objects'. In: *Nature Physics* 9.7 (2013), pp. 400–404.

[3] J. Borregaard, M. Zugenmaier, J.M. Petersen, H. Shen, G. Vasilakis, K. Jensen, E.S. Polzik, and A.S. Sørensen. 'Scalable photonic network architecture based on motional averaging in room temperature gas'. In: *Nature communications* 7.1 (2016), pp. 1–9.

[4] B. Julsgaard, J. Sherson, J. I. Cirac, J. Fiurášek, and E. S. Polzik. 'Experimental demonstration of quantum memory for light'. In: *Nature* 432.7016 (2004), pp. 482–486.

[5] K. B. Dideriksen, R. Schmieg, M. Zugenmaier, and E. S. Polzik. 'Room-temperature single-photon source with near-millisecond built-in memory'. In: *Nature communications* 12.1 (2021), pp. 1–7.

[6] L.M. Duan, Lukin M.D., and P. Cirac J.I nad Zoller. 'Long-distance quantum communication with atomic ensembles and linear optics'. In: *Nature* 414.413-418 (2001).

[7] W. Wasilewski, K. Jensen, H. Krauter, J. J. Renema, M. V. Balabas, and E. S. Polzik. 'Quantum Noise Limited and Entanglement-Assisted Magnetometry'. In: *Phys. Rev. Lett.* 104 (13 Mar. 2010), p. 133601.

[8] K. B. Dideriksen. *'A room-temperature single-photon source in built-in memory'*. Ph.D.' Thesis, University of Copenhagen. 2021.

[9]   M. V. Balabas, T. Karaulanov, M. P. Ledbetter, and D. Budker. 'Polarized Alkali-Metal Vapor with Minute-Long Transverse Spin-Relaxation Time'. In: *Phys. Rev. Lett.* 105 (7 Aug. 2010), p. 070801.

[10] R. Schmeig. *'Observation of non-classical photon pairs from room-temperature atomic ensembles through suppression of four-wave mixing and classical noise sources.'* Masters' Thesis, University of Copenhagen. 2019.

[11] C. J. Foot. *Atomic Physics*. First. Oxford University Press Inc., New York, 2005.

[12] D. A. Steck. *'Cesium D Line Data'*. Available online at http://steck.us/alkalidata. (revision 2.2.1, 21 November 2019).

[13] B Julsgard. *'Entanglement and Quantum Interactions with Macroscopic Gas Samples'*. Ph.D. Thesis, University of Copenhagen. 2003.

[14] J. Arnbak. *'Magnetocardiography and Eddy-Current Imaging using an Optical Cesium Vapor Magnetometer'*. Masters' Thesis, University of Copenhagen. 2017.

[15] D. J. Griffiths. *Introduction to Quantum Mechanics*. First. Upper Saddle River, NJ : Pearson Prentice Hall, 1995, pp. 257–58.

[16] K. Hammerer, A. S. Sørensen, and E. S. Polzik. 'Quantum interface between light and atomic ensembles'. In: *Rev. Mod. Phys.* 82 (2 Apr. 2010), pp. 1041–1093.

[17] A. Fabricant. *'Quantum-limited optical magnetometry with cesium microcells'*. Masters' Thesis, University of Copenhagen. 2014.

[18] H. Zheng, W. Quan, X. Liu, Y. Chen, and L. Jixi. 'Determination of Atomic Number Densities of 87 Rb and 3 He Based on Absorption Spectroscopy'. In: *Chinese Physics Letters* 31 (2014), pp. 103203–103203.

[19] K. A. Kluttz, T. D. Averett, and B. A. Wolin. 'Pressure broadening and frequency shift of the D_1 and D_2 lines of Rb and K in the presence of ^{3}He and N_2'. In: *Phys. Rev. A* 87 (3 Mar. 2013), p. 032516.

[20] M. Kristensen, F. J. Blok, M. A. van Eijkelenborg, G. Nienhuis, and J. P. Woerdman. 'Onset of a collisional modification of the Faraday effect in a high-density atomic gas'. In: *Phys. Rev. A* 51 (2 Feb. 1995), pp. 1085–1096.

[21] G. Labeyrie, C. Miniatura, and R. Kaiser. 'Large Faraday rotation of resonant light in a cold atomic cloud'. In: *Physical Review A* 64.3 (2001), p. 033402.

[22] Mellish B. *Faraday effect [picture]*. https://commons.wikimedia.org/wiki/File:Faraday-effect.svg, 2007.

[23] Brian Julsgaard, Jacob Sherson, JL Sørensen, and Eugene S Polzik. 'Characterizing the spin state of an atomic ensemble using the magneto-optical resonance method'. In: *Journal of Optics B: Quantum and Semiclassical Optics* 6.1 (2003), p. 5.

[24] D. A. Steck. *'Quantum and Atom Optics'*. Available online at http://steck.us/teaching. (revision 0.13.11, 7 April 2022).

[25] R. Schmeig. *'Summary Note on cell fabrication and testing'*. University of Copenhagen. 2022.

[26] M. Enault-Dautheribes. *'Optically Narrowed Laser Towards the Implementation of a Single-Photon Source on the D1 Line of Caesium'*. Masters' Thesis, University of Copenhagen. 2017.

[27] Thorlabs. *Thorlabs Beam Analyzing Software. BP209-VIS/M Operating manual.* Eighth. Thorlabs, 2021.

[28] R. Schmeig. *'Coherent dynamics of atomic vapors'*. University of Copenhagen. 2018.

[29] NIST. *'Fundamental Phisical Constants'*. Available online at http://https://physics.nist.gov/cuu/Constants/index.html. (last visited 3 May 2022).

[30] E. Hetch. *Optics*. Fourth. Addison Wesley, 2002, p. 704.

[31] Sergey V. E. 'Exact solution of Helmholtz equation for the case of non-paraxial Gaussian beams'. In: *Journal of King Saud University - Science* 27.3 (2015), pp. 198–203.

[32] P. Hariharan and P.A. Robinson. 'The Gouy phase shift as a geometrical quantum effect'. In: *Journal of Modern Optics* 43.2 (1996), pp. 219–221.

[33] O. Svelto and D. C. Hanna. *Principles of lasers*. Fifth. Springer, 1998.

[34] CVI Melles Griot. 'Gaussian beam optics'. In: *Gaussian Beam Opt* 2.1 (2009).

[35] Mellish B. *Hermite-Gaussian [picture]*. https://commons.wikimedia.org/wiki/File:Hermite-gaussian.png. 200.

[36] J. Alda. 'Laser and Gaussian beam propagation and transformation'. In: *Encyclopedia of optical engineering* 999 (2003).

[37] P. Duggal. *'An Experimental Study of Rim Formation in Single-Shot Femtosecond Laser Ablation of Borosilicate Glass'*. Masters' Thesis, The University of Texas. 2006.

[38] G. F. Marshall. *Laser Beam Scanning*. First. Routledge, 1985.

[39] Mellish B. *Gaussian Beam Waist [picture]*. https://commons.wikimedia.org/wiki/File:GaussianBeamWaist.svg. 2009.

[40] K. Laskei and C. Boone. 'Flat-top laser beams: Their uses and benefits'. In: *Laser Focus World* (Dec. 2021).

[41] S. Rung, M. Rexhepi, C. Bischoff, and R. Hellmann. 'Laserscribing of Thin Films Using Top-Hat Laser Beam Profiles'. In: *Journal of Laser Micro / Nanoengineering* 8 (Dec. 2013), p. 309.

[42] K. Sun, L. Zhu, K. Cady-Pereira, C. Chan Miller, K. Chance, L. Clarisse, P.-F. Coheur, G. González Abad, G. Huang, X. Liu, *et al. A physics-based approach to oversample multi-satellite, multispecies observations to a common grid*. Vol. 11. 12. Copernicus GmbH, 2018, pp. 6679–6701.

[43] G. Račiukaitis, E.s Stankevičius, P. Gečys, M.s Gedvilas, C. Bischoff, E. Jäger, U. Umhofer, and F. Völklein. 'Laser Processing by Using Diffractive Optical Laser Beam Shaping Technique.' In: *Journal of laser micro/nanoengineering* 6.1 (2011).

[44] F. M. Dickey, L. S. Weichman, and R. N. Shagam. 'Laser beam shaping techniques'. In: *High-Power Laser Ablation III*. Vol. 4065. International Society for Optics and Photonics. 2000, pp. 338–348.

[45] F. M. Dickey. *Laser beam shaping: theory and techniques*. Marcel dekker, Inc., 2000.

[46] P. Blair, M. Currie, N. Trela, H. J. Baker, E. Murphy, D. Walker, and R. McBride. 'Field mappers for laser material processing'. In: *Laser Resonators, Microresonators, and Beam Control XVIII*. Vol. 9727. International Society for Optics and Photonics. 2016, 97270S.

[47] J. Cordingley. 'Application of a binary diffractive optic for beam shaping in semiconductor processing by lasers'. In: *Applied optics* 32.14 (1993), pp. 2538–2542.

[48] A. Möhl and U. Fuchs. 'Exploring the unlimited possibilities of modular aspheric Gauss to top-hat beam shaping'. In: *Advanced Optical Technologies* 5.3 (2016), pp. 201–210.

[49] S. Zhang, G. Neil, and M. Shinn. 'Single-element laser beam shaper for uniform flat-top profiles'. In: *Optics Express* 11.16 (2003), pp. 1942–1948.

[50] L.A. Romero and F.M. Dickey. 'Lossless laser beam shaping'. In: *JOSA A* 13.4 (1996), pp. 751–760.

[51]   S. Katz, N. Kaplan, and I. Grossinger. 'Using Diffractive Optical Elements: DOEs for beam shaping–fundamentals and applications'. In: *Optik & Photonik* 13.4 (2018), pp. 83–86.

[52]   Holo/Or Ltd. *Top-Hat beam shaper. Installation manual.* Second. Holo/Or Ltd., 2020.

[53]   EKSMA Optics. *GTH-4-2.2FA Gauss-to-Top-Hat Beam Shaping Lens.* Second. EKSMA Optics, 2020.

[54]   TOPAG Lasertechnik. *Product Technical Description. Gauss-to-Top-Hat Beam Shaper Lens. GTH-4-2.2.* Second. TOPAG Lasertechnick, 2012.

[55]   TOPAG Lasertechnik. *GTH-S-4.0-2.0, Gaussian to Top Hat shaper*. First. TOPAG Lasertechnick.

[56]   FLIR. *FLIR BLACKFLY® GIGE VISION datasheet*. FLIR, 2017.

[57]   Newport Corporation. *'Achromatic doublet Lenses'*. Available online at https://www.newport.com/n/achromatic-doublet-lenses. (last visit, 5 May 2022).

[58]   J. W. Goodman. *Introduction to Fourier Optics*. Second. The McGraw-Hill Companies, INC., 1996.

Ray transfer matrix analysis - ABCD matrix formalism

As described in [58], under the paraxial approximation, any optical transformation to a light ray (entering a surface, reflecting on a mirror, crossing a lens, etc., even travelling in a medium) can be described as a 2x2 matrix transformation applied to a vector that describes the incident light. These matrices are the so-called *ray transfer matrices*. The light vectors are composed of two components, the transverse coordinate of the ray y and the angle at which the beam enters the system θ.

Under the paraxial approximation, the relation between two rays (y_1, θ_1) and (y_2, θ_2) is linear and can be written as

$$\begin{cases} y_2 = Ay_1 + D\hat{\theta}_1 \\ \hat{\theta}_2 = Cy_1 + D\hat{\theta}_1 \end{cases} \tag{A.1}$$

In matrix notation

$$\begin{pmatrix} y_2 \\ \hat{\theta}_2 \end{pmatrix} = \begin{pmatrix} A & B \\ C & D \end{pmatrix} \begin{pmatrix} y_1 \\ \hat{\theta}_1 \end{pmatrix} \tag{A.2}$$

Where the ABCD matrix describes the transformation. Some examples of these matrices are [58]:

- **Propagation through a free space d of index n**

$$\mathbf{S} = \begin{pmatrix} 1 & \frac{d}{n} \\ 0 & 1 \end{pmatrix} \tag{A.3}$$

- **Propagation through a lens with focal distance f**

$$\mathbf{L} = \begin{pmatrix} 1 & 0 \\ -\frac{1}{f} & 1 \end{pmatrix} \tag{A.4}$$

- **Reflection of a mirror with effective radius R_e**
  The effective radius is defined as $R_e = R cos\phi$ where R is the radius of curvature
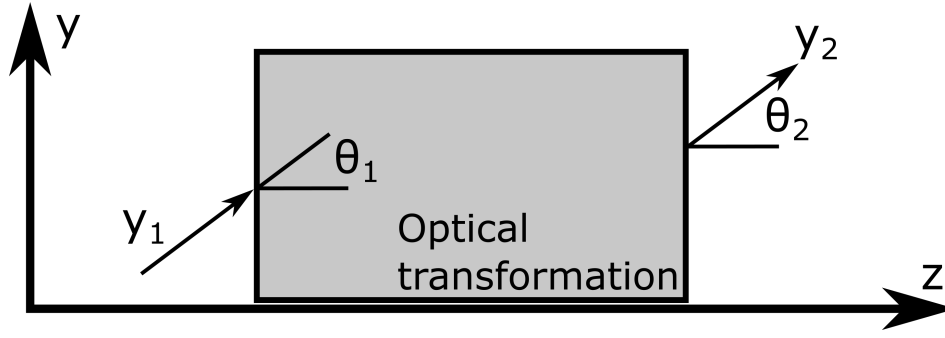
Figure A.1.: Representation of ray transfer analysis. The grey box represents any optical transformation.

and ϕ is the angle of incidence.

$$\mathbf{M} = \begin{pmatrix} 1 & 0 \\ -\frac{2}{R_e} & 1 \end{pmatrix} \qquad (A.5)$$

Different transformations might be taken into account at the same time. For example, the transformation of a beam travelling a distance d_1, crossing a lens with f_1, and travelling a distance d_2 can be represented as

$$\begin{pmatrix} y_2 \\ \hat{\theta}_2 \end{pmatrix} = \mathbf{S}_2 \mathbf{L}_1 \mathbf{S}_1 \begin{pmatrix} y_1 \\ \hat{\theta}_1 \end{pmatrix} \qquad (A.6)$$

Collimation images

Images of the two collimation approaches described in .

1. Collimation setup where the distance between the focusing lens and collimation lens is $D = 153\,\text{mm}$. In this approach, the TH waist does not match the predictions at the EFL, and the collimation of the beam is noticeable. In $180\,\text{mm}$ the TH waist changes $\Delta w \sim 40\,\mu\text{m}$.

2. Collimation setup where the distance between the focusing lens and collimation lens is $D = 156\,\text{mm}$. In this approach, the TH waist matches the predictions at the EFL, and the convergence of the beam is noticeable. In $70\,\text{mm}$, the TH waist changes $\Delta w \sim 160\,\mu\text{m}$.

B.1   D=153 mm
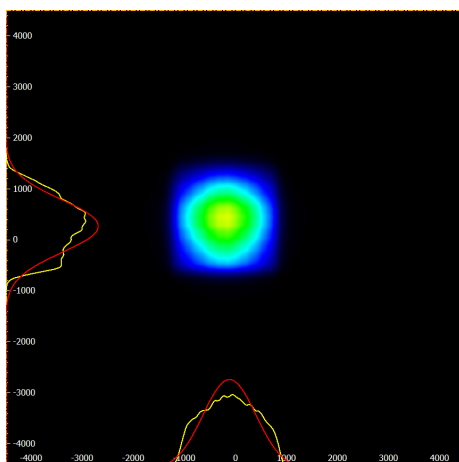
(a) $d = 330$ mm, $w = 2066\,\mu$m
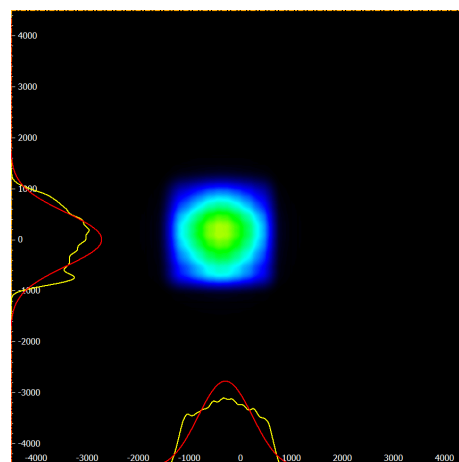
(b) $d = 370$ mm, $w = 2075\,\mu$m
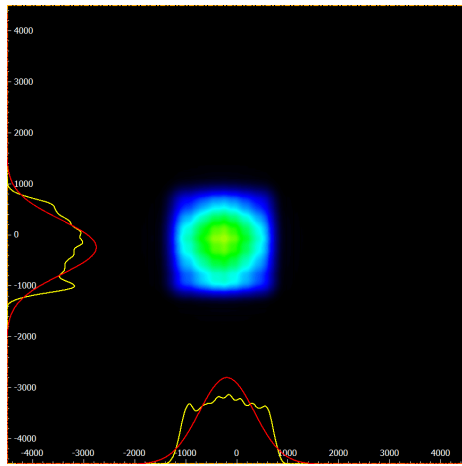
(a) $d = 410$ mm, $w = 2076\,\mu$m
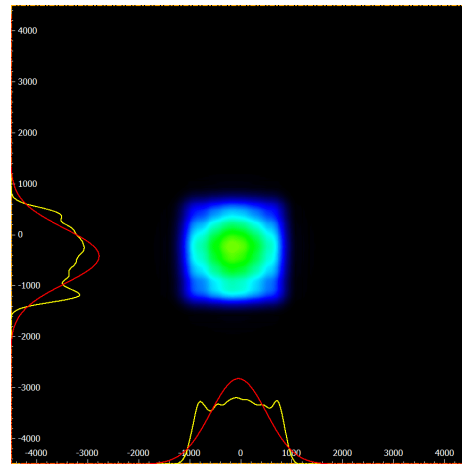
(b) $d = 440$ mm, $w = 2083\,\mu$m
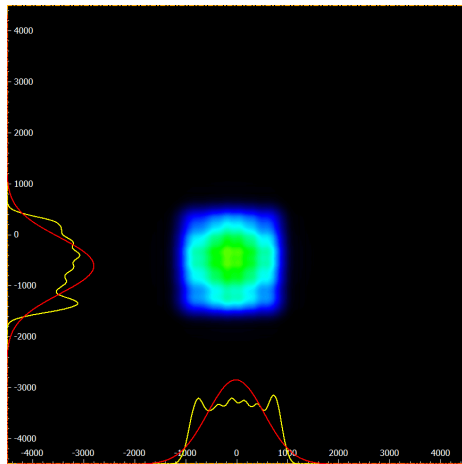
(c) $d = 480$ mm, $w = 2088\,\mu$m
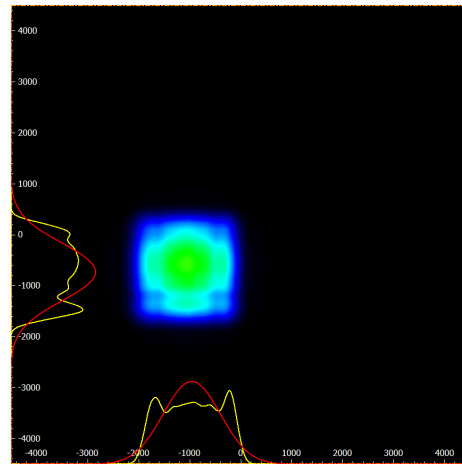
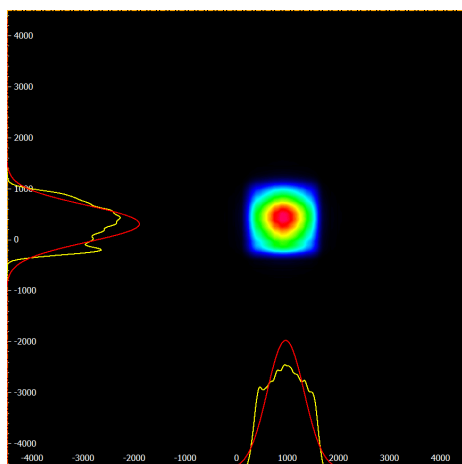**(d)** $d = 520$ mm, $w = 2089\,\mu$m
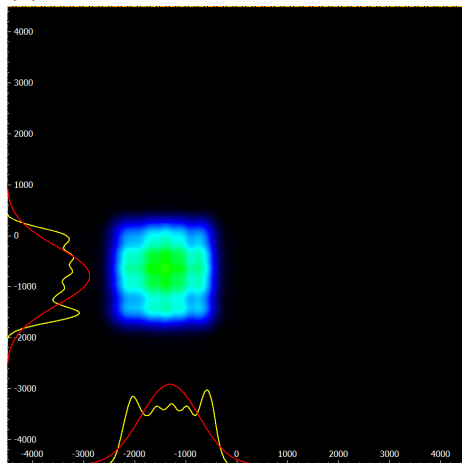
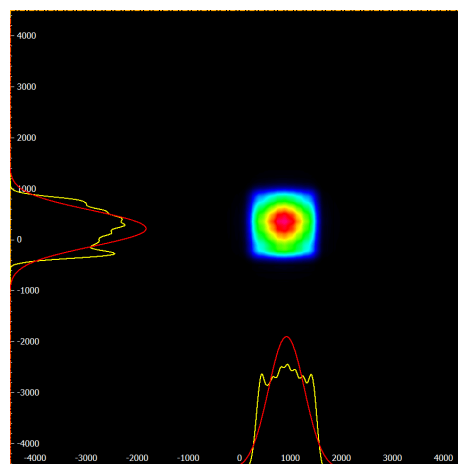**(e)** $d = 560$ mm, $w = 2105\,\mu$m
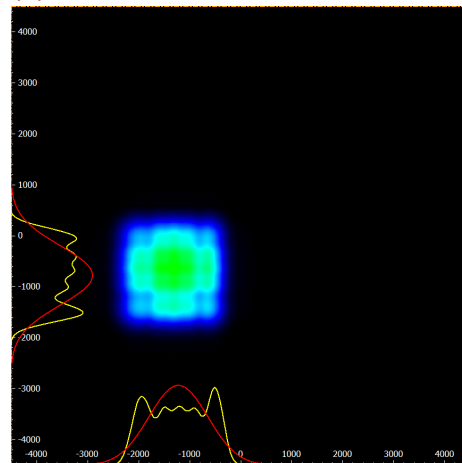
(f) $d = 590$ mm, $w = 2115\,\mu$m

Figure B.2.: Collimation of the TH with a separation of 153 mm between the focusing lens and the collimation lens. In the plots d is the distance where the image was taken in respect to the collimation lens, and w is the parameter that represents the squared waist of the profile ($w_{TH} = w \times w$)
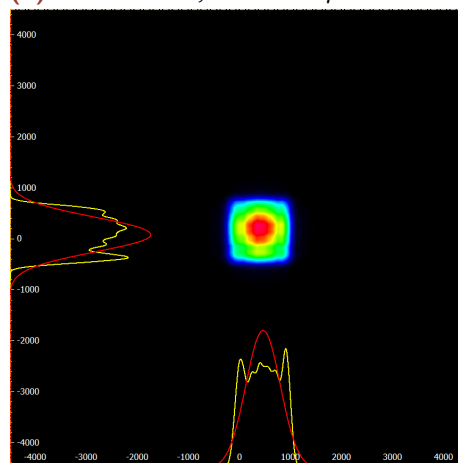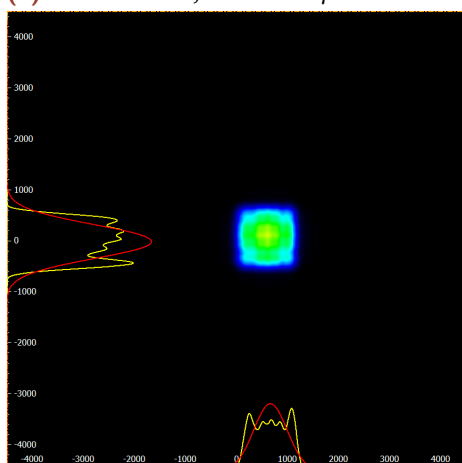
B.2 D=156 mm

(a) $d = 270$ mm, $w = 1410\,\mu$m

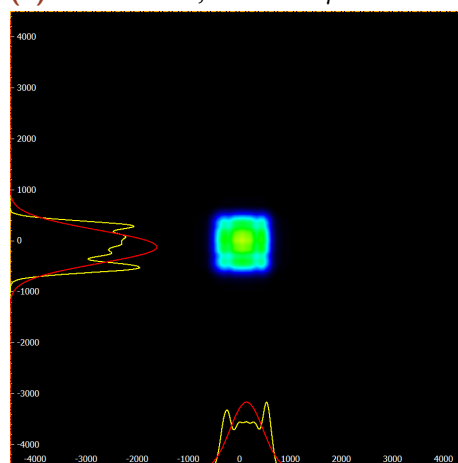(b) $d = 290$ mm, $w = 1348\,\mu$m
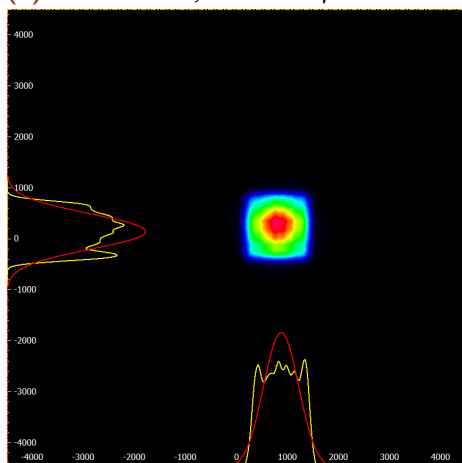
(c) $d = 310$ mm, $w = 1300\,\mu$m

(d) $d = 320$ mm, $w = 1260\,\mu$m

(e) $d = 340$ mm, $w = 1210\,\mu$m

(f) $d = 360$ mm, $w = 1190\,\mu$m

Figure B.3.: Collimation of the TH with a separation of 156 mm between the focusing lens and the collimation lens. In the plots d is the distance where the image was taken in respect to the collimation lens, and w is the parameter that represents the squared waist of the profile ($w_{TH} = w \times w$)